THE GEOLOGICAL SOCIETY OF AMERICA®

Early and middle Miocene ice sheet dynamics in the Ross Sea: Results from integrated core-log-seismic interpretation

Lara F. Pérez[1,2,3,†], Laura De Santis[2,§], Robert M. McKay[3,§], Robert D. Larter[1,§], Jeanine Ash[4,§], Phil J. Bart[5,§], Gualtiero Böhm[2,§], Giuseppe Brancatelli[2,§], Imogen Browne[6,§], Florence Colleoni[2,§], Justin P. Dodd[7,§], Riccardo Geletti[2,§], David M. Harwood[8,§], Gerhard Kuhn[9,§], Jan Sverre Laberg[10,§], R. Mark Leckie[11,§], Richard H. Levy[3,12,§], James Marschalek[13,§], Zenon Mateo[14,§], Timothy R. Naish[3,§], Francesca Sangiorgi[15,§], Amelia E. Shevenell[6,§], Christopher C. Sorlien[16,§], Tina van de Flierdt[13,§], and International Ocean Discovery Program Expedition 374 Scientists[14,§]

[1]*British Antarctic Survey, Cambridge CB3 0ET, UK*
[2]*National Institute of Oceanography and Applied Geophysics, Trieste 34010, Italy*
[3]*Victoria University of Wellington, Wellington 6140, New Zealand*
[4]*Department of Earth, Environmental and Planetary Sciences, Rice Natural Sciences, Rice University, Houston, Texas 77005, USA*
[5]*Department of Geology & Geophysics, College of Science, Louisiana State University, Baton Rouge, Louisiana 70803, USA*
[6]*College of Marine Science, University of South Florida, St. Petersburg, Florida, 33701 USA*
[7]*Department of Geology and Environmental Geosciences, Northern Illinois University, DeKalb, Illinois 60115, USA*
[8]*Department of Earth and Atmospheric Sciences, University of Nebraska, Lincoln 68588-0340, USA*
[9]*Alfred Wegener Institute, Helmholtz Centre for Polar and Marine Research, Bremerhaven 27570, Germany*
[10]*UiT The Arctic University of Norway, Tromsø 9037, Norway*
[11]*Department of Geosciences, University of Massachusetts Amherst, Amherst, Massachusetts 01003-9297, USA*
[12]*GNS Science, Wellington, Lower Hutt 5040, New Zealand*
[13]*Department of Earth Science and Engineering, Imperial College London, South Kensington Campus, London SW7 2AZ, UK*
[14]*International Ocean Discovery Program, Texas A&M University, College Station, Texas 77845, USA*
[15]*Department of Earth Sciences, Marine Palynology and Paleoceanography, Utrecht University, Utrecht, The Netherlands*
[16]*University of California, Santa Barbara, California, 93106 USA*

ABSTRACT

Oscillations in ice sheet extent during early and middle Miocene are intermittently preserved in the sedimentary record from the Antarctic continental shelf, with widespread erosion occurring during major ice sheet advances, and open marine deposition during times of ice sheet retreat. Data from seismic reflection surveys and drill sites from Deep Sea Drilling Project Leg 28 and International Ocean Discovery Program Expedition 374, located across the present-day middle continental shelf of the central Ross Sea (Antarctica), indicate the presence of expanded early to middle Miocene sedimentary sections. These include the Miocene climate optimum (MCO ca. 17–14.6 Ma) and the middle Miocene climate transition (MMCT ca. 14.6–13.9 Ma). Here, we correlate drill core records, wireline logs and reflection seismic data to elucidate the depositional architecture of the continental shelf and reconstruct the evolution and variability of dynamic ice sheets in the Ross Sea during the Miocene. Drill-site data are used to constrain seismic isopach maps that document the evolution of different ice sheets and ice caps which influenced sedimentary processes in the Ross Sea through the early to middle Miocene. In the early Miocene, periods of localized advance of the ice margin are revealed by the formation of thick sediment wedges prograding into the basins. At this time, morainal bank complexes are distinguished along the basin margins suggesting sediment supply derived from marine-terminating glaciers. During the MCO, biosiliceous-bearing sediments are regionally mapped within the depocenters of the major sedimentary basin across the Ross Sea, indicative of widespread open marine deposition with reduced glacimarine influence. At the MMCT, a distinct erosive surface is interpreted as representing large-scale marine-based ice sheet advance over most of the Ross Sea paleo-continental shelf. The regional mapping of the seismic stratigraphic architecture and its correlation to drilling data indicate a regional transition through the Miocene from growth of ice caps and inland ice sheets with marine-terminating margins, to widespread marine-based ice sheets extending across the outer continental shelf in the Ross Sea.

INTRODUCTION

The early to middle Miocene (23 Ma to 11.6 Ma) was a time of highly-variable global

Lara F. Pérez https://orcid.org/0000-0002-6229-4564

[†]Corresponding author: larrez@bas.ac.uk.

[§]ldesantis@inogs.it (De Santis); robert.mckay@vuw.ac.nz (McKay); rdla@bas.ac.uk (Larter); ja39@rice.edu (Ash); pbart@lsu.edu (Bart); gbohm@inogs.it (Böhm); gbrancatelli@inogs.it (Brancatelli); imogenbrowne@usf.edu (Browne); fcolleoni@inogs.it (Colleoni); jdodd@niu.edu (Dodd); rgeletti@inogs.it (Geletti); dharwood1@unl.edu (Harwood); gerhard.kuhn@awi.de (Kuhn); jan.laberg@uit.no (Laberg); mleckie@geo.umass.edu (Leckie); r.levy@gns.cri.nz (Levy); j.marschalek18@imperial.ac.uk (Marschalek); mateo@iodp.tamu.edu (Mateo); timothy.naish@vuw.ac.nz (Naish); F.Sangiorgi@uu.nl (Sangiorgi); ashevenell@usf.edu (Shevenell); christopher.sorlien@ucsb.edu (Sorlien); tina.vandeflierdt@imperial.ac.uk (van de Flierdt); expedition_374_participants@iodp.tamu.edu.

GSA Bulletin; https://doi.org/10.1130/B35814.1; 11 figures; 2 tables; 1 supplemental file.

climate, punctuated by large oscillations in eustatic sea level (~30–60 m) associated with major changes in polar ice volume (Haq et al., 1987; Flower and Kennett, 1994; Zachos et al., 2001; Kominz et al., 2008, 2016; John et al., 2011; Miller et al., 2020). Deep-sea benthic foraminifer $\delta^{18}O$ isotopes exhibit ~1‰ increase at ca. 14 Ma, termed the middle Miocene climate transition (MMCT), one of the three major climate transitions of the Cenozoic, which was accompanied by significant Southern Ocean cooling and inferred expansion of ice sheets in Antarctica (Shackleton and Kennett, 1975; Flower and Kennett, 1994; Zachos et al., 2001; Shevenell et al., 2004, 2008; Miller et al., 2020). Geological studies support intensification of high latitude cooling and ice sheet expansion during the MMCT, with geomorphic, geological, and paleo-ecological evidence for the transition to a cold, hyper-arid polar landscape in the Transantarctic Mountains (Brook et al., 1995; Summerfield et al., 1999; Sugden and Denton, 2004; Lewis et al., 2006, 2008; Warny et al., 2009; Gulick et al., 2017; Balter-Kennedy et al., 2020). The ~1‰ far-field deep-sea $\delta^{18}O$ isotopic increase was originally associated with the development of a permanent East Antarctic Ice Sheet (EAIS) and the first major marine-based expansion of the West Antarctic Ice Sheet (WAIS), also supported by terrestrial evidence from Antarctica (Shackleton and Kennett, 1975; Kennett, 1977; Sugden et al., 1993; Sugden and Denton, 2004; Lewis et al., 2006). However, drilling results from the Antarctic Drilling Project (ANDRILL), the Antarctic Cenozoic history CIROS drilling project, Cape Roberts Drilling Project (CRP), and the predecessor drilling programs to the International Ocean Discovery Program (IODP) indicate that the history of marine-based sectors of both the WAIS and EAIS is likely more complicated (Barrett, 1989; Bart, 2003; Barrett, 2007; McKay et al., 2009; Naish et al., 2009; Escutia et al., 2011; Cook et al., 2013; Holbourn et al., 2013; Patterson et al., 2014; Levy et al., 2016; Gulick et al., 2017; Sangiorgi et al., 2018; Wilson et al., 2018). Paired with high-resolution seismic stratigraphic frameworks, these drill records provide direct evidence of both widespread advance and large-scale retreat of marine-based ice sheets across the Antarctic continental shelf following the MMCT (De Santis et al., 1995; Bart, 2003; Gulick et al., 2017; Levy et al., 2019).

The MMCT is also notable as it represents the termination of a prolonged period of relative warmth (e.g., Flower and Kennett, 1994; Holbourn et al., 2014; Kender et al., 2014), known as the Miocene climate optimum (MCO; ca. 17–14.6 Ma). Data-model comparisons suggest that global temperatures during the MCO were at least 3–4 °C higher than present, with greater warming in Antarctica due to polar amplification (e.g., Shevenell et al., 2004; You et al., 2009; Goldner et al., 2014; Levy et al., 2016; Sangiorgi et al., 2018). Paleoenvironmental data from the Transantarctic Mountains and offshore Ross Sea drill cores indicate a vegetated landscape influenced by significant volumes of glacial meltwater (Lewis et al., 2006, 2008; Warny et al., 2009; Feakins et al., 2012; Levy et al., 2016, 2019). Consequently, climates were periodically warm enough to allow for widespread surface melt of the terrestrial margins of the Antarctic ice sheets. Models constrained by geological data indicate that ice sheets across Antarctica may have retreated to the hinterland of its terrestrial margins during peak interglacial periods of the MCO (Gasson et al., 2016; Levy et al., 2016). However, the nature and timing of maximum glacial extent during and prior to the MCO remains ambiguous.

Importantly, the paleotopography of West Antarctica may have changed significantly through the Cenozoic, due to active rifting, thermal subsidence, and glacial erosion (Leckie and Webb, 1983; Savage and Ciesielski, 1983; Cande et al., 2000; Bart, 2003; Wilson et al., 2012; Gasson et al., 2016; Granot and Dyment, 2018; Paxman et al., 2019), leading to a much larger terrestrial extent of the Antarctic continent during the Miocene, including existence of isolated islands on the Ross Sea continental shelf as late as 14 Ma (Paxman et al., 2019). Models using idealized reconstructions of the paleotopography indicate that sea level variations of up to ~40 m are feasible if the ice sheets expanded to the outer paleo-continental shelf edge around most of the Antarctic continent, but also retreated far-inland during peak warm interglacials (Gasson et al., 2016). These model-based assessments are smaller than the deep-sea geochemical estimates of ice volume variance and far-field sea level estimates of ~60 m (Zachos et al., 2001; Kominz et al., 2008; Cramer et al., 2011; John et al., 2011; Holbourn et al., 2014; Miller et al., 2020).

The vast continental shelf of the Ross Sea has evolved under the influence of the ice sheets and the sediment supply sourced from both East and West Antarctica. It is thus ideally suited for ground-truthing when maximum ice sheet advance occurred prior to, during, and after the MCO. According to ice sheet models, the Antarctic ice sheets are nearing their maximum volume when ice is grounded in the Ross Sea outer continental shelf (Gasson et al., 2016; Colleoni et al., 2018). Therefore, improved stratigraphic constraints in the Ross Sea will better allow for the histories of the WAIS and EAIS to be deconvolved (e.g., Anderson and Bartek, 1992; Brancolini et al., 1995; Bart and Anderson, 2000; Licht et al., 2005; Golledge et al., 2013; Tinto et al., 2019).

A dense network of seismic reflection data constrained by drill core observations provides the opportunity to discriminate between distinct erosion/deposition patterns caused by locally grounded ice caps on regional bathymetric highs, versus large-scale ice sheet advances across the continental shelf. Here, we aim to constrain the regional spatial extent of ice sheet and ice cap advances and retreats that influenced sedimentation in the middle to outer continental shelf of the central Ross Sea during the early and middle Miocene. We correlate seismic records with drill-site physical properties and lithostratigraphy from Deep Sea Drilling Project (DSDP) sites 272 and 273 (Hayes et al., 1975), and IODP Site U1521 (McKay et al., 2019) (Fig. 1). The correlation of wireline and core logs with reflection seismic data reveals marked temporal and spatial variability in the erosional surfaces and sedimentary depocenters on the Ross Sea continental shelf, which we interpret as evidence of a highly variable ice sheet volume throughout the early and middle Miocene.

REGIONAL BACKGROUND

The present-day bathymetry of the Ross Sea continental shelf is a result of the combined tectonic, climatic, and glacial evolution that has led to the development of several sedimentary basins, which are elongated perpendicular to the margin (Fig. 1A). The late rifting phase of the West Antarctic rift system evolved since ca. 45 Ma associated with basaltic volcanism and resulting in block faulting and further uplift of the Transantarctic Mountains (e.g., Cooper and Davey, 1987, 1991; Fitzgerald, 1992; Davey and Brancolini, 1995; Cande et al., 2000; Granot and Dyment, 2018). Continental stretching led to variable crustal thickness across the Ross Sea and differential subsidence/uplift rates (Savage and Ciesielski, 1983; Karner et al., 2005), which together with sediment and ice loading have changed the bathymetry of the Ross Sea continental shelf by several hundred meters since the Oligocene–Miocene boundary (Paxman et al., 2019).

The Ross and Iselin banks are inferred to form the tectonic boundary between East and West Antarctic lithosphere according to magnetic and gravity models (Tinto et al., 2019) and separate eastern and western Ross Sea domains (Fig. 1A). In the eastern Ross Sea, the Little America, Whales, and Glomar Challenger basins are separated by the Houtz and Hayes banks. In the western Ross Sea, Pennell, Joides, and Drygalski basins are separated by Pennell and Crary-Mawson banks, which are composed

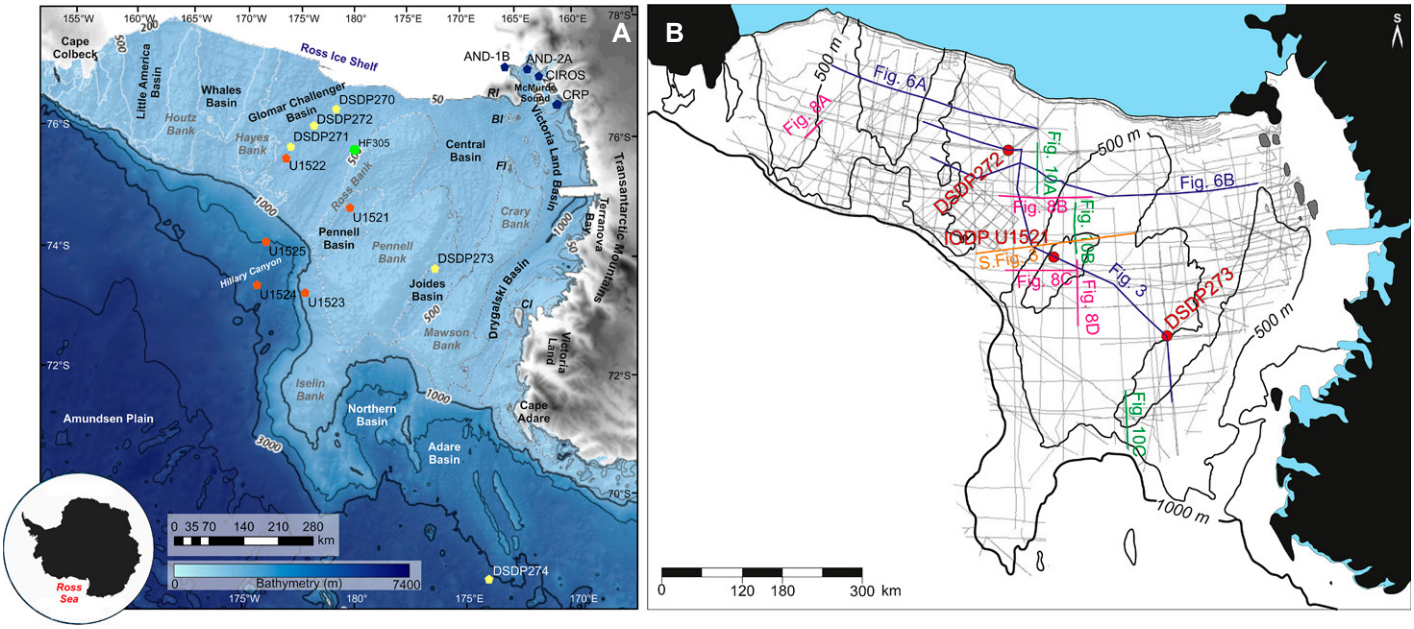

Figure 1. (A) Overview of the Ross Sea bathymetry, Antarctica (Arndt et al., 2013). BI—Beaufort Island; FI—Franklin Island; RI—Ross Island; Cl—Coulman Island. Colored dots represent legacy drill sites, with the exception of the green dot, which is heat flow Site HF305 (Sato et al., 1984). (B) Simplified map of the Ross Sea continental shelf. Depth contours define the modern continental shelf edge and the limits of banks and basins as named in Figure 1A. Grey lines are the navigation tracks of seismic reflection profiles used in this work. The locations of the seismic profiles shown in the figures are highlighted. Note that the westernmost Ross Sea (Drygalski and Victoria Land basins) is out of the scope of the present work. AND—ANDRILL Antarctic Drilling Project; CIROS—Antarctic Cenozoic history CIROS drilling; CRP—Cape Roberts Drilling Project; DSDP—Deep Sea Drilling Project; IODP—International Ocean Discovery Program.

of sedimentary strata. Landwards, the Pennell and Joides basins merge into the Central Basin, which is separated from McMurdo Sound and Victoria Land Basin by a chain of volcanic edifices in the surroundings of Franklin, Beaufort, and Ross islands (Fig. 1A).

The broad seismic-stratigraphy of the Ross Sea was first established by Cooper and Davey (1987) and subsequently refined in the 1990s by the Scientific Committee on Antarctic Research (SCAR) Antarctic Offshore Stratigraphy Project (ANTOSTRAT), which correlated the available seismic lines with the DSDP Leg 28 drill sites (Fig. 1A). ANTOSTRAT provided comprehensive regional maps of the wide-range stratigraphic architecture (Brancolini et al., 1995). The sedimentary record was subdivided into two sequences. The underlying sequence comprised syn-rift sediments of inferred Mesozoic to early Eocene age (Cooper and Davey, 1987). The upper sequence contains six major unconformities named Ross Sea unconformities (RSU) from RSU1 (youngest) to RSU6 (oldest) that have been attributed to several origins, including tectonic events, glacial erosion, and sea level oscillations (Hinz and Block, 1984; Bartek et al., 1991; Alonso et al., 1992; Anderson and Bartek, 1992; Busetti et al., 1993; Brancolini et al., 1995; Cooper et al., 1995; De Santis et al., 1995). The eight intervening seismic sequences were termed Ross Sea seismic sequences (RSS), from top to bottom, RSS8 to RSS1, respectively (Fig. 2) (Cooper et al., 1995).

The glacial histories of the eastern and western Ross Sea have been dominantly influenced by the WAIS and EAIS, respectively. Ice streams that periodically extend into the Ross Sea drain large portions of the EAIS and the WAIS (e.g., Shipp et al., 1999; Denton and Hughes, 2002; Licht et al., 2005; Golledge et al., 2013; Anderson et al., 2014; Perotti et al., 2017). Seismic profiles reveal ice streams carved troughs across the paleo-continental shelf during ice sheet advances (Alonso et al., 1992; Anderson and Bartek, 1992, Anderson et al., 2019), and the large discharge of sediments built trough-mouth-fans on the paleo-continental slope (e.g., De Santis et al., 1999; Bart et al., 2000; Kim et al., 2018). Models constrained by provenance data indicate that ice flow has undergone multiple configuration changes during the most recent glacial cycles (e.g., Golledge et al., 2013).

Sediments recovered in the western Ross Sea CRP sites CRP-2/2A, and CRP-1, and ANDRILL AND-2A indicate at least 32 cycles of ice growth and decay adjacent to the Transantarctic Mountains through the beginning of early Miocene (20.2–17.4 Ma). During this time, termini of EAIS outlet glaciers periodically advanced close to, or across, the southern Victoria Land Basin (see Fielding, 2018 for a recent synthesis) and surface temperatures varied from significantly colder to a few degrees warmer than today (Levy et al., 2016). During the latest early Miocene (ca. 17–15.9 Ma) fewer episodes of grounded ice advance are recorded (Fielding et al., 2011; Passchier et al., 2011). The drill Site AND-2A also indicates ice volume fluctuated through the MCO, and a series of warm intervals with durations of 0.1–0.2 m.y. were separated by generally cold intervals of longer, but variable, duration (Fielding, 2018).

Sedimentary facies in the AND-1B Site indicate that marine and terrestrial ice sheet margins were characterized by significant turbid meltwater input during the late Miocene (ca. 11.6–5.3 Ma) (McKay et al., 2009). Sediment starvation during glacial periods and deposition of diatom ooze during interglacial periods indicate a shift toward a polar setting with oscillating ice sheets during Plio-Pleistocene time (McKay et al., 2012). Seismic sequences indicate a minimum of seven large-scale ice sheet advances toward the continental shelf edge during Plio-Pleistocene (e.g., Anderson and Bartek, 1992; Bart and Anderson, 2000; Kim et al., 2018), while a minimum of 38 cycles of marine-based

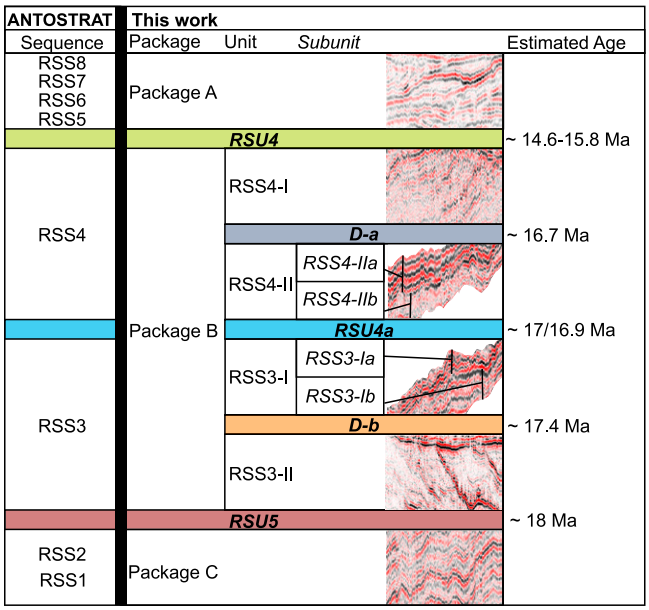

Figure 2. Seismic facies distinguished on the seismic packages, units, and subunits of the Ross Sea as defined in this work and correlated to ANTOSTRAT seismic sequences as in Brancolini et al. (1995).

ice sheet advance and retreat are preserved in the AND-1B Site (Fig. 1A) in the inner continental shelf region over the past 5 m.y. (Naish et al., 2009).

DATA AND METHODS

The results presented in this work combine several geophysical techniques, summarized below. The bathymetric data for the base map (Fig. 1) have been extracted from the International Bathymetric Chart of the Southern Ocean (Arndt et al., 2013).

Regional Seismic Database and Interpretation

An extensive seismic dataset is available for the continental shelf of the Ross Sea (Fig. 1B). The database contains multichannel (MCS) and single channel (SCS) reflection seismic profiles acquired by international partners during several decades of research (Table 1). Data quality and resolution are therefore variable. Most of the MCS lines are available in stack version at the SCAR Seismic Data Library System for Cooperative Research (https://sdls.ogs.trieste.it). Details on the processing sequence of MCS and SCS profiles implemented for the manuscript are included in the Supplemental Material[1].

The MCS and SCS profiles have been imported into an IHS-Kingdom project to facilitate seismic-stratigraphic analyses. The seismic interpretation criteria adopted the basic analytical methods of seismic stratigraphy (e.g., Payton, 1977). Therefore, major stratigraphic discontinuities were identified from reflection configurations indicative of unconformities and their correlative conformities, which in many cases are expressed as high amplitude reflections that present a regional signature. Two of the main stratigraphic discontinuities identified in ANTOSTRAT interpretations and maps (Brancolini et al., 1995; Cooper et al., 1995), referred to as RSU4 and RSU5, have been examined and reinterpreted. Reinterpretation of the ANTOSTRAT stratigraphic boundaries of the same name (Supplemental Fig. S4; see footnote 1) was based on taking into consideration new available seismic data, wireline, and core logs from DSDP and

[1]Supplemental Material. Additional information regarding methods (Reflection seismic processing, Drill-site measurements, Core-log-seismic correlations, Spatial Velocity calculations, and Reflection Tomography model) and regional stratigraphy descriptions, as well as detailed considerations regarding the opal distribution and depth. Please visit https://doi.org/10.1130/GSAB.S.14356205 to access the supplemental material, and contact editing@geosociety.org with any questions.

TABLE 1. MAIN ACQUISITION PARAMETERS OF THE SEISMIC DATASET IN THE ROSS SEA, USED FOR THE MAPPING IN THIS WORK

Line group	Number of lines	Recording length	Source	Receiver	Sampling interval	Samples per trace	Institution and year
ATC82B	7	9	Bolt Air Guns 35.54 l	Prakla-seismos 48 ch	4	3000	IFP / France / 1982
BGR80	26	6	'U' 24 Air Guns 23.45 l	Prakla-seismos 48 ch	4	2000	BGR / Germany / 1980
I06290	22	3	2 Air Guns 11.64 l	48 ch	2		OGS / Italy / 2005
IT17RS	40	6	2 GI Guns 6.88 l	Single-channel	1		OGS / Italy
IT88AR	6	5	14 Air Guns 45.16 l	Prakla-seismos 96 ch	2	8000	OGS / Italy /1988
IT89AR	24	6	2 Air Guns 45.16 l	Prakla-seismos 120 ch	4	12,000	OGS / Italy /1989
IT91AR	2	8	2 × 20 Air Guns 74.8 l	Prakla-seismos 120 ch	2	8000	OGS / Italy /1991
IT94AR	6	8	2 × 20 Air Guns 74.8 l	Prakla-seismos 120 ch	2	8000	OGS / Italy /1994
KSL12/14	7	8	GI Air Gun 3.44 l	Geometrics 96 ch	2	2500	KORDI / Korea
L284AN	18	10	5 Air Guns 21.5 l	GUS HDDR 4200 24 ch	2	10,000	USGS / USA / 1984
NBP0306	44	4	GI Air Gun 3.44 l	Geometrics 96 ch	2	2500	University of Santa Barbara / USA / 2004
NBP0401	60	4	GI Air Gun 3.44 l	Geometrics 96 ch	2	2500	University of Santa Barbara / USA / 2004
NBP0701	30	12	6 GI Air Guns 20.6 l		2	4000	University of Santa Barbara / USA / 2007
NBP0802	18	2	GI Air Gun 3.44 l	Single-channel	2	2000	Louisiana State University / USA / 2008
NBP0803	20	2	GI Air Gun 3.44 l	Single-channel	2	2000	Louisiana State University / USA / 2008
NBP1502	25	2	GI Air Gun 3.44 l	Geometrics 96 ch	2	2000	Louisiana State University / USA / 2015
NBP31	42	3	4 GI Air Guns 1.7 l	45 ch			University of Santa Barbara / USA
NBP9601	36	4	GI Air Gun 3.44 l	Geometrics 96 ch	2	2500	University of Santa Barbara / USA / 1996
NBP9602	10	10	GI Air Gun 3.44 l	Geometrics 96 ch	2	2500	University of Santa Barbara / USA / 1996
NBP9702	29	6	GI Air Gun 3.44 l	Geometrics 96 ch	2	2500	University of Santa Barbara / USA / 1997
PD90	51	4	GI Air Gun 2.46 l	Single-channel	2	4000	Rice University / USA / 1990
SEV87	17	7	Bolt Air Gun 10.0 l	Progress-2 24 ch	4	6000	Sevmorgeologia / Russia / 1987
SEV89	17	6	Bolt Air Gun 10.0 l	Progress-2 24 ch	4	6000	Sevmorgeologia / Russia / 1989
TH82	9	9	Bolt Air Gun 9.2 l	Ministreamer 24 ch	4	10,000	JNOC /Japan / 1982
TH91	10	7	2 Water Guns 13.11 l	DFS-V 24 ch	4	9000	JNOC /Japan / 1991
TH92	8	5	3/4 GI Guns 7.4 l	DFS-V 48 ch	4	11,000	JNOC /Japan / 1991
TH95	8	9.5	4 GI Guns 9.8 -13.7 l	AESOP 168 ch	4	14,000	JNOC /Japan / 1995

Notes: Recording length is given in seconds two-way travel-time, whereas sampling interval is given in milliseconds. ch—channels; BGR—German Federal Institute for Geosciences and Natural Resources; IFP—French Institute of Petroleum; JNOC—Japan National Oil Corporation; KORDI—Korea Ocean Research and Development Institute; OGS—National Institute of Oceanography and Applied Geophysics; USGS—U.S. Geological Survey.

IODP drill sites, and updated age models. Major differences between the mapped RSUs and those published in ANTOSTRAT are described in the Supplemental Material. The remapping of surfaces associated with the ANTOSTRAT RSUs is used to define three seismic packages in this work, Package A, Package B, and Package C from top to bottom (Figs. 2 and 3).

Equally, the discontinuity interpreted here as RSU4a correlates with the same named discontinuity identified by De Santis et al. (1995) with major re-adjustments related to the latest available data. Within Package B, surface RSU4a separates ANTOSTRAT sequences RSS4 (above) and RSS3 (below). Additional

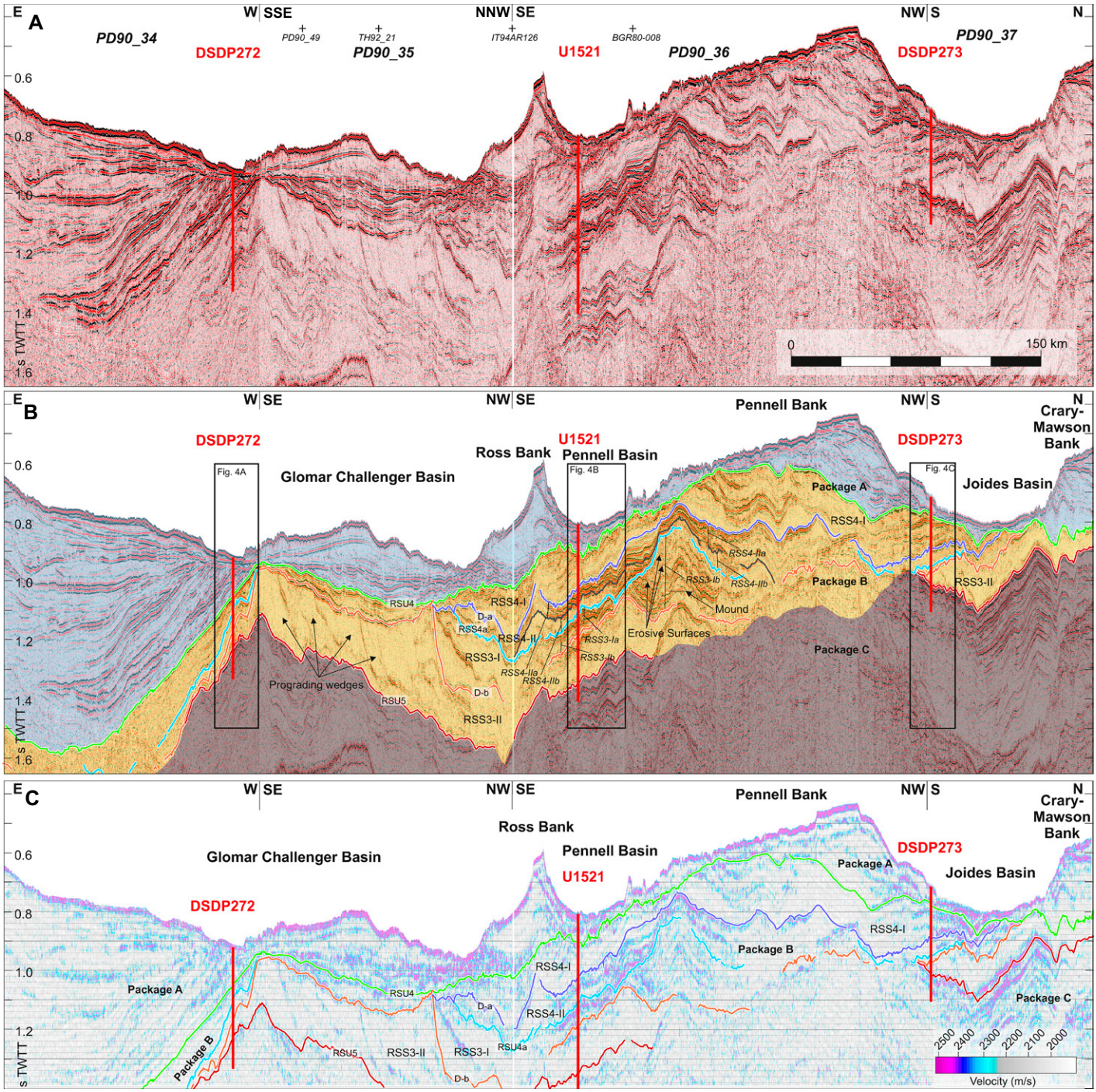

Figure 3. (A) Seismic profile across the middle continental shelf of the Ross Sea, Antarctica, composed of the single channel profiles PD90_34, PD90_35, PD90_36, and PD90_37. Deep Sea Drilling Project (DSDP) sites 272 and 273, and International Ocean Discovery Program Site U1521 locations are marked. The crossing line points are marked. (B) Interpreted seismic packages, units, and subunits and stratigraphic discontinuities over the composite profile shown in (A). See profile location in Figure 1B (blue line). TWTT—two-way travel-time. The location of the profile segments shown in Figure 4 are marked with black boxes. (C) Spatial velocity distribution along the composite profile (A) based on the multi-attribute analysis of Hampson Russell software (Supplemental Material; see footnote 1).

stratigraphic discontinuities D-a (in RSS4) and D-b (in RSS3) not defined by ANTOSTRAT have now been mapped in this work through integration of wireline and core logging data with the SCS profiles (Fig. 2). These discontinuities allow division of Package B into four seismic units defined as RSS4-I and RSS4-II from top to bottom in sequence RSS4, and RSS3-I and RSS3-II from top to bottom in sequence RSS3 (Figs. 2 and 3). Additionally, within these seismic units several seismic subunits are distinguished based on their seismic facies. These are referred to as RSS4-IIa and RSS4-IIb, from top to bottom in the stratigraphic column; and RSS3-Ia and RSS3-Ib, following the same criteria (Figs. 2 and 3). The seismic units and subunits of Package B identify shifts in glacial erosion and sedimentary depocenters through the deposition of the package, and form the main focus of this work.

The regional seismic facies have been interpreted after Anderson and Bartek (1992) and De Santis et al. (1995) and the prograding/aggrading sequences have been interpreted following Cooper et al. (1995). At the bottom of the sedimentary record, the top of the acoustic basement has been mapped through interpretations of several MCS profiles on which processing has been improved with respect to the ANTOSTRAT version. However, further work considering magnetic and gravimetry data, as well as major reprocessing of seafloor multiple reflections would be needed to develop an accurate map of the igneous and metamorphic basement. Therefore, only the general morphology of the basement top is considered here for mapping purposes.

Contour maps of surfaces and thicknesses of seismic sequences and units are presented in two-way travel-time (TWTT). They have been created by flex gridding interpolation with 100 × 100 m cell size. According to the data distribution and the area of interest of this study, the mapping limits were set at Cape Colbeck to the east and Crary-Mawson Bank and the southern volcanic edifices to the west. The edge of the Ross Ice Shelf marks the natural landward limit and the oceanward boundary is formed by the edge of the present-day continental shelf roughly following the 1000 m bathymetric contour line (Fig. 1). No deep drilling sites exist within the eastern Ross Sea domain, i.e., to the east of Glomar Challenger Basin, and therefore the resolution and constraints are reduced in this area and dependent on the accuracy of seismic surface correlations.

Drill-Site Measurements and Corrections

IODP Site U1521, drilled during Expedition 374 in 2018, and DSDP sites 272 and 273, drilled during Leg 28 in 1973, are used in this study to correlate the seismic stratigraphy. The sites are located along the present-day middle continental shelf of the Ross Sea (Fig. 1), and the age models developed from biostratigraphic and paleomagnetic techniques show relatively expanded sequences of Miocene sediments (Hayes et al., 1975; Bart, 2003; McKay et al., 2019). However, it should be noted that all age models are subject to future refinement through improved resolution of biostratigraphic observations and development of a consistent biostratigraphic framework between recent and legacy cores that is beyond the scope of this study. Indeed, the seismic stratigraphic mapping presented in this work is intended to help inform the development of new chronostratigraphies in these sites as it allows for the identification of erosional surfaces as well as regional ties of sediment packages, and this helps to constrain whether sedimentary successions that have significant thickness in a drill core in one part of the region may be missing in the drill cores from another area.

IODP Site U1521 is located at 75°41.0351′S, 179°40.3108′W in Pennell Basin at 562 m water depth (wd) (Fig. 1). Core and wireline (downhole) logging measurements were completed in the site to 650.1 m below seafloor (mbsf), above which depth average core recovery was 63%. Details on the coring techniques and logging tools are provided in McKay et al. (2019). DSDP Site 272 is located at 77°07.62′S, 176°45.61′W in Glomar Challenger Basin at 629 m wd (Fig. 1). 37% core recovery was obtained from the total 443 mbsf penetrated (Hayes et al., 1975). DSDP Site 273 is located at 74°32.29′S, 174°37.57′E in Joides Basin at 495 m wd (Fig. 1). The site penetrated to 346.5 mbsf with 25% sediment recovery (Hayes et al., 1975). Nearly all the cores in DSDP sites 272 and 273 were core logged for P-wave velocity (V_p). In addition, logged wet bulk density values were determined along the cores from the analog gamma ray attenuation porosity evaluation (GRAPE) records by linear interpolation (Hayes and Frakes, 2004a, 2004b).

The variability of the physical properties between the three sites was analyzed in Hampson Russell-EMERGE™ commercial software package (Calgary, Alberta, Canada). Differences in data quality and resolution between the wireline and core logging outputs, and different lithological classification schemes between DSDP and IODP expeditions have been taken into consideration in the present study while comparing the data of the three sites (Fig. 4). Wireline and core logs have been resampled to 5 m by applying a running average, to obtain records with vertical resolution approaching that of the seismic data while minimizing loss of variability (Fig. 5). Physical properties measured through core and downhole logging techniques at Site U1521 present similar trends with local differences in absolute values (Fig. 5C). Compressional velocity measured from discrete core samples correlates well with the multi-sensor core logger and wireline downhole logging P-wave measurements (McKay et al., 2019). Core and downhole magnetic susceptibility trends differ at certain depths due to the absence of full temperature correction in the downhole logging (McKay et al., 2019). Core logging measurements of density values (wet bulk density) are lower than wireline logging values (mean difference ~0.21 g/cm^3). The correlation between wireline downhole logged density and core logged wet bulk density has been calculated and used to correct the anomalously low wet bulk density values of DSDP sites 272 and 273 cores as detailed in the Supplemental Material. The corrected densities are used in this work for the DSDP sites. Density values have been used to calculate porosities (ϕ) and acoustic impedance (I_p), as detailed in the Supplemental Material.

Magnetic susceptibility, natural gamma radiation, and resistivity have been measured at Site U1521 by both wireline downhole logging (used hereafter but otherwise noticed) and multi-sensor core logging (Fig. 5C). Water saturation (S_w) along the stratigraphic column is calculated at Site U1521 on the basis of porosity (ϕ) and resistivity (R_t) measurements (Supplemental Material).

The formation microscanner (FMS)-sonic tool string was run at Site U1521 (McKay et al., 2019). FMS images provide a high-resolution image of the resistivity-conductivity condition of the sediment surrounding the borehole. Site U1521 FMS images have been considered in the present work to provide an indication of the heterogeneity at restricted intervals of the sedimentary record.

Core-Log-Seismic Ties

Core-log-seismic ties allow the relevant variability of the wireline and core logs to be extended to a broader area. Logging values from relevant physical properties have been tied with *RV Polar Duke* cruise PD90 SCS profiles (Fig. 4). Site U1521 ties with profile PD90_36 (Fig. 4B). Borehole seismic check-shot measurements were obtained at Site U1521 allowing the direct time-depth correlation for the core-log-seismic tie as described in the Supplemental Material.

The absence of wireline downhole logs and check-shot data from DSDP sites 272 and 273 limits the core-seismic correlation. DSDP Site 272 ties with SCS profile PD90_34, whereas DSDP Site 273 is on PD90_37 (Figs. 3A and 3C). Time-depth correlation for these sites has been calculated using the stacking velocities

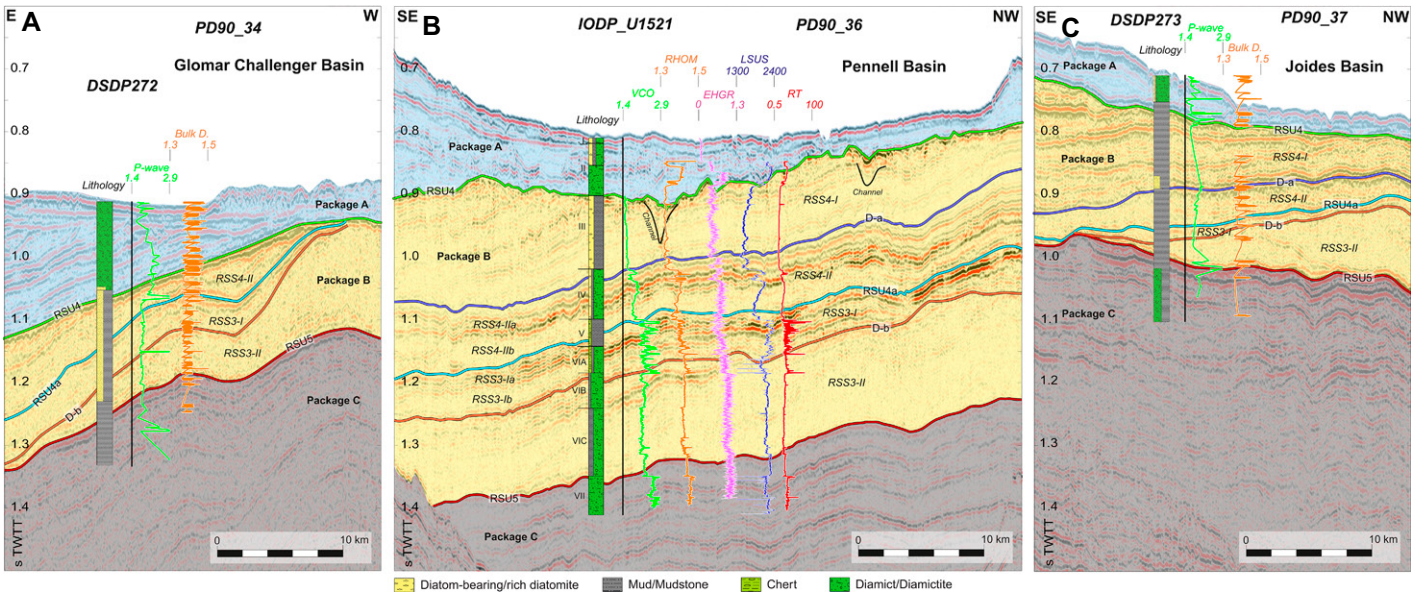

Figure 4. Core-log-seismic correlation of (A) reclassified lithology, P-wave velocity (km/s), and wet bulk density (Bulk D) (g/cm^3) data of core logging in Deep Sea Drilling Project (DSDP) Site 272 with profile PD90_34; (B) lithology and lithostratigraphic units from McKay et al. (2019), velocity (VCO, km/s), density (RHOM, g/cm^3), gamma ray (EHGR, American Petroleum Institute), magnetic susceptibility (LSUS), and resistivity (RT, Ohm·m) data of downhole logging in International Ocean Discovery Program (IODP) Site U1521 with profile PD90_36; and (C) reclassified lithology, P-wave velocity (km/s) and wet bulk density (Bulk D) (g/cm^3) data of core logging in DSDP Site 273 with profile PD90_37. The interpreted seismic packages and stratigraphic discontinuities are shown. The black vertical lines show the actual locations of the sites, while the logs are laterally projected. See locations in Figure 3B. TWTT—two-way travel-time.

of the crossing MCS profiles (BGR80-002 and BGR80-001, respectively to DSDP sites 272 and 273) following Brancolini et al. (1995) and detailed in the Supplemental Material. The adjusted time-depth correlations were imported in the IHS-Kingdom project to proceed with the core-log-seismic ties (Figs. 3B and 4).

Velocity Analyses

Anomalously high compressional velocity values have been measured at restricted intervals of the drilled sites (Figs. 4 and 5). Spatial velocity distribution and reflection tomography analyses have been created along seismic profiles proximal to the sites in order to explore the implications of the velocity variability (Supplemental Material). However, the velocity analysis results have not been further used for seismic depth conversions due to the large uncertainties in the regional velocity models.

The compressional velocities from the wireline and core logging of the three sites have been extrapolated along a composite SCS profile formed by lines PD90_34, PD90_35, PD90_36, and PD90_37. The resulting 2-D profile shows the spatial distribution of velocities along the present-day middle continental shelf of the central Ross Sea (Fig. 3C). This 2-D velocity distribution has been obtained from multi-attribute analysis in Hampson Russell software as detailed in the Supplemental Material.

Travel-time inversion tomography has been performed along the MCS profile IT94AR126 in the surroundings of IODP Site U1521. The methodology and model analyses are detailed in the Supplemental Material. The tomography model provides a large-scale velocity field in depth (Supplemental Fig. S3; see footnote 1). Variability in velocity values highlights lateral changes within the seismic packages and sequences.

CORE-LOG-SEISMIC CORRELATION: THE STRATIGRAPHIC RECORD

The regional sedimentary record of the continental shelf of the Ross Sea east of Crary-Mawson Bank forms two major depocenters in the eastern (>3 s TWTT) and western (>2 s TWTT) sectors (Fig. 3B). Between them, a SE-NW area of thinner cover runs from the southwest Glomar Challenger Basin to the northern Pennell Bank. In this work, three major seismic packages are identified in the sedimentary record, Package A, Package B, and Package C, from the seafloor downwards in the stratigraphic column (Figs. 2 and 3B). They are distinguished on the basis of the correlation between the available MCS and SCS profiles and the wireline and core logging data of DSDP Site 272, IODP Site U1521, and DSDP Site 273 (Fig. 4). Package A is characterized with thick depocenters (>2.5 s TWTT) on the outer continental shelf of the eastern Ross Sea formed by prograding wedges (Figs. 2, 3A, 3B, 6, and 7). In addition, grounding zone wedges have been previously described embedded on the sedimentary sequences contained in this package (Bart and De Santis, 2012). Package C is regionally formed by widespread aggradational medium amplitude, high lateral continuity, and stratified reflections in the upper part (Figs. 2, 3A, and 3B). However, sparse mounded-elongated bodies can be identified in the upper part of the package along the northern Pennell Bank and the southern Glomar Challenger Basin. They are formed by continuous reflections tilted toward the central part of Pennell and Glomar Challenger basins, respectively (Fig. 8D). These mounded bodies are ~0.35 s TWTT high and ~5 km long. A general description of Package A and Package C distribution, seismic facies and physical properties is included in the Supplemental Material of this manuscript, while Package B and its stratigraphic boundaries are the core focus of this work.

Package B: RSU4 to RSU5

At the top of Package B, discontinuity RSU4 is represented by a high amplitude reflection that truncates the underlying sedimentary record

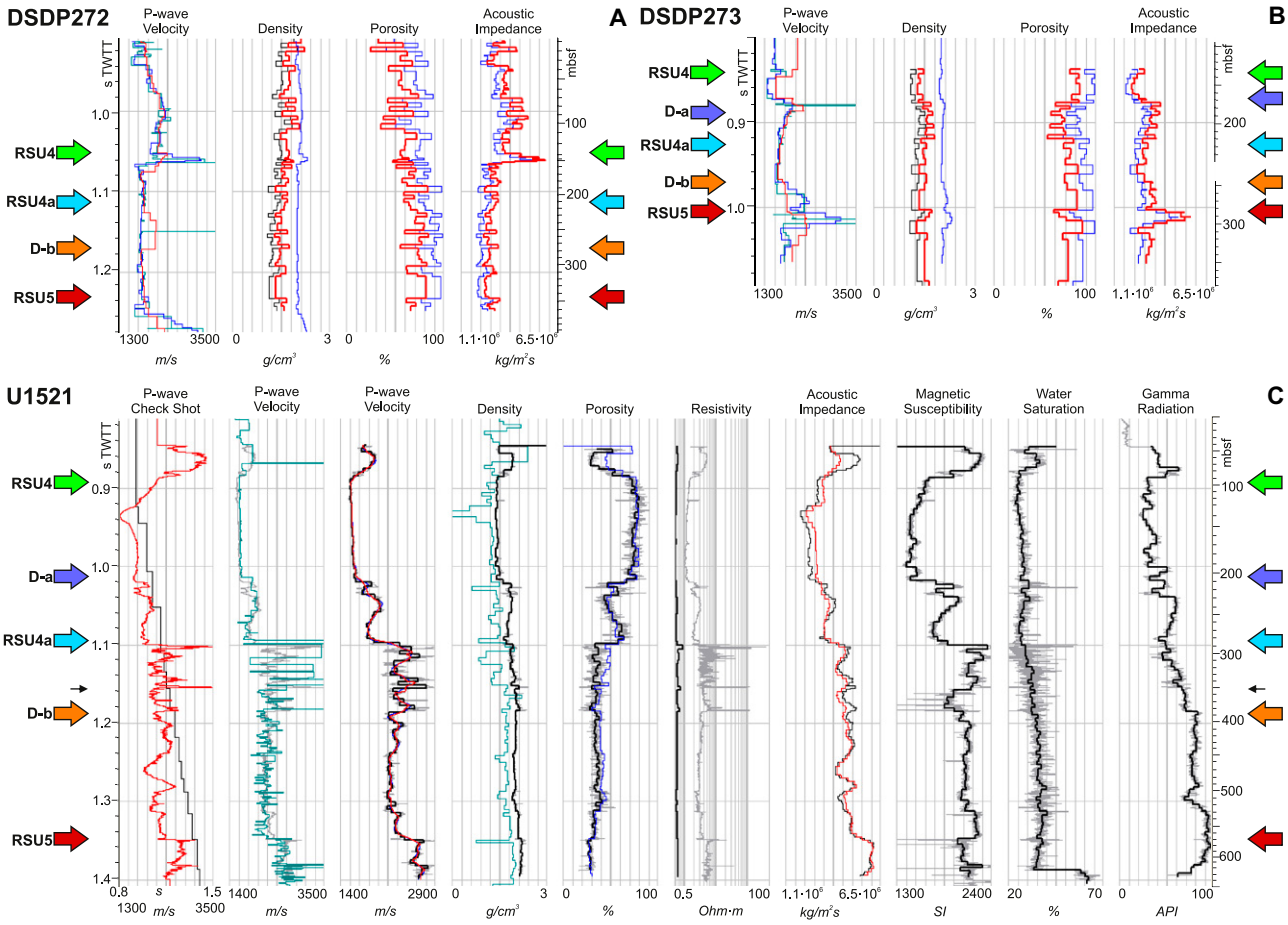

D

		Package B				
	Package A	*RSS4-I*	*RSS4-II*	*RSS3-I*	*RSS3-II*	Package C
P-wave velocity (m/s)	1600 – 1900	1600 – 2200	1900 – 2100	1700 – 1900	1800 – 2350	~2700
Density (g/cm^3)	1.0 – 2.7	1.3 – 1.8	1.6 – 2.1	1.3 – 2.2	~1.8	~2.0
Porosity (%)	30 – 60	70 – 85	44 – 85	30 – 80	38 – 83	30 – 85
Resistivity (Ω·m)	1.1 – 3.0	0.9 – 1.1	1.4 – 2.0	2.1 – 5.4	1.7 – 2.2	~3
Magnetic susceptibility (SI)	1600 – 2280	1400 – 1670	1720 – 2030	1860 – 2370	2110 – 2240	~2075
Natural gamma radiation (API)	4 – 63	30 – 51	50 – 60	50 – 84	83 – 86	77 – 95
Water saturation (%)	25 – 37	25 – 29	25 – 30	29 – 32	37 – 40	33 – 38

Figure 5. Logged physical properties of the three sites along the middle continental shelf of the Ross Sea, Antarctica, with stratigraphic discontinuity locations as colored arrows. The thin black arrow points to the location of the base of RSS3-Ia at International Ocean Discovery Program (IODP) Site U1521. (A) Core logging from Deep Sea Drilling Project (DSDP) Site 272. P-wave: velocity data (green) resampled to 5 m (blue) and with running average filter (red); Density: resampled to 5 m (black), corrected with IODP Site U1521 densities cross-plot relation (red) and calculated from velocities following Gardner's law (blue); Porosity resampled to 5 m: calculated from density values (blue) and from corrected density values (red); Acoustic impedance resampled to 5 m: calculated from core logged velocity and density (blue), and from core logged velocity and corrected density (red). (B) Core logging from DSDP Site 273, using same processing and color scheme as DSDP Site 272 (A). (C) Downhole wireline logged (gray) and core logged (green) data from IODP Site U1521. Solid black lines show the downhole data resampled to 5 m. Check shot trend (black) and downhole P-wave corrected with check shots (red); P-wave velocity: downhole logged (gray) and core logged (green); downhole logged P-wave (gray), resampled to 5 m (black), with high-pass frequency filter at 50 Hz and a low-pass frequency filter at 60 Hz in time domain (blue), and resampled with a running average (red); Density: downhole logged (gray), core logged (green), downhole logged resample to 5 m (black); Porosity: downhole logged (gray) resampled to 5 m (black) and calculated from downhole logged densities resampled to 5 m (blue); Resistivity: downhole logged (gray) resampled to 5 m (black); Acoustic impedance calculated from downhole logged velocity and density (red) resampled to 5 m (black); Magnetic susceptibility: downhole logged (gray) resampled to 5 m (black); Water saturation calculated from downhole logged porosity and resistivity (gray) resampled to 5 m (black); Gamma radiation: downhole logged (gray) resampled to 5 m (black). (D) Average range of the main physical properties in the interpreted seismic packages and units from wireline logging at IODP Site U1521 and core logging at DSDP sites 272 and 273. TWTT—two-way travel-time; mbsf—meters below seafloor.

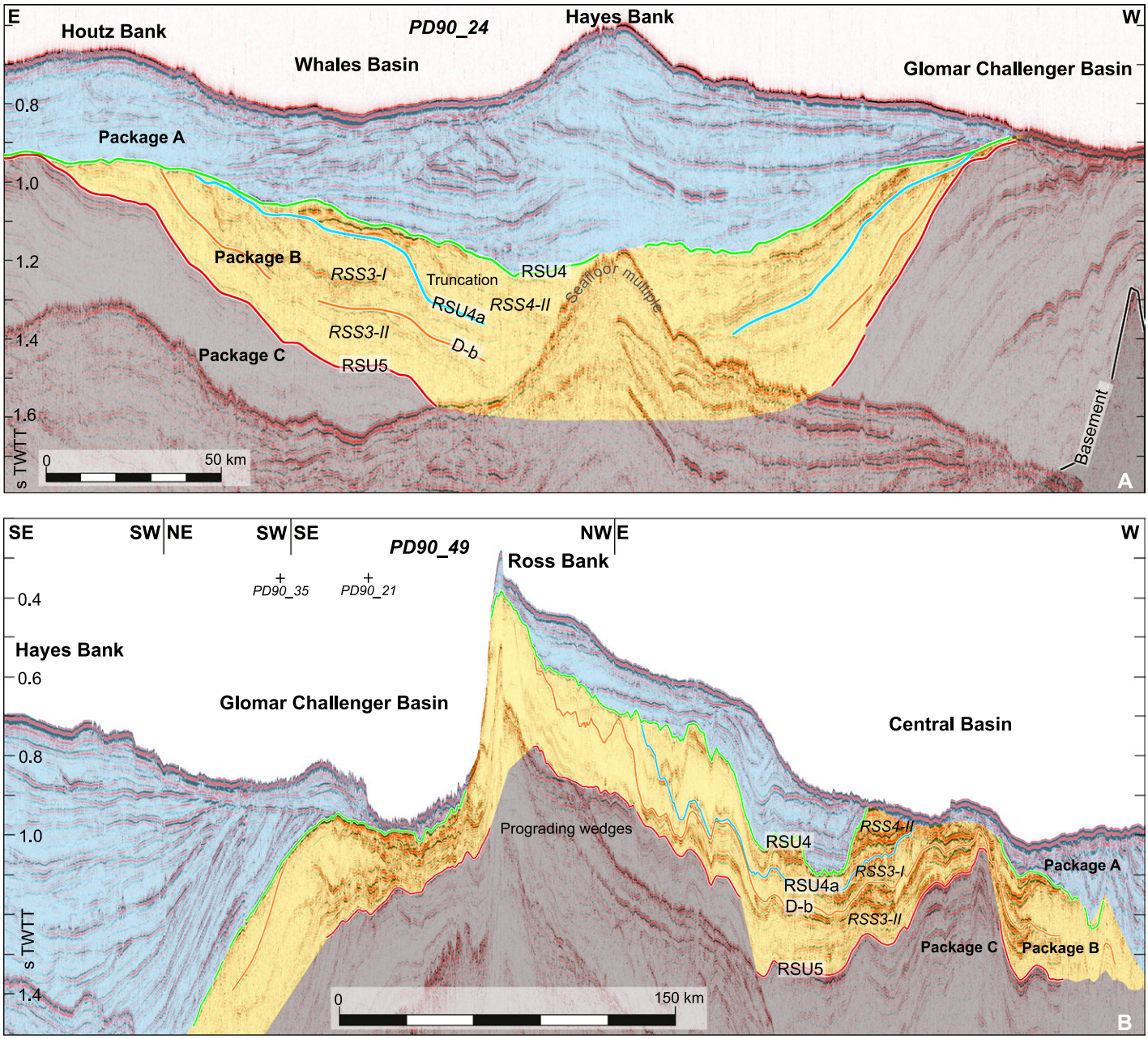

Figure 6. Single channel seismic profiles (A) PD90_24 across the inner continental shelf of the eastern Ross Sea, Antarctica from Whales Basin to Glomar Challenger Basin; and (B) PD90_49 across the inner continental shelf of the western Ross Sea from Hayes Bank to Crary Bank. The interpreted sedimentary packages and discontinuities are shown. See location in Figure 1B (blue lines). TWTT—two-way traveltime. The crossing line points are marked.

through a broad area. It is laterally continuous and can be traced regionally, although it is affected locally by channel-like morphologies (Figs. 3B and 6). The U-shape channels formed in association with RSU4 are over 0.05 s TWTT deep and 12 km wide, whereas the V-shape channels carve ~0.08 s TWTT (Fig. 4B). RSU4 marks a regional change in the seismic facies from higher reflectivity above to lower reflectivity below. However, lateral changes in the seismic facies lead to a local reversal of this pattern. RSU4 is identified at 126, 110, and 60 mbsf at DSDP Site 272, IODP Site U1521, and DSDP Site 273, respectively, representing a sharp change in P-wave, density, and magnetic susceptibility trends (Fig. 5). Regionally, RSU4 is deeper in the eastern Ross Sea (2 s TWTT), forming a broad depression in the central part of the continental shelf that deepens rapidly toward the modern shelf edge (Fig. 7). In contrast, to the west of Ross Bank, RSU4 is relatively shallow (0.8 s TWTT), particularly on the southeastern Ross Bank and northeastern Pennell Bank (<0.6 s TWTT). In this region, RSU4 forms focused troughs oriented in a NE-SW direction, which deepen toward the Central Basin (>1 s TWTT).

In general, Package B is thickest to the northeast where maximum thickness of 0.8 s TWTT is recorded in the present-day outer shelf of

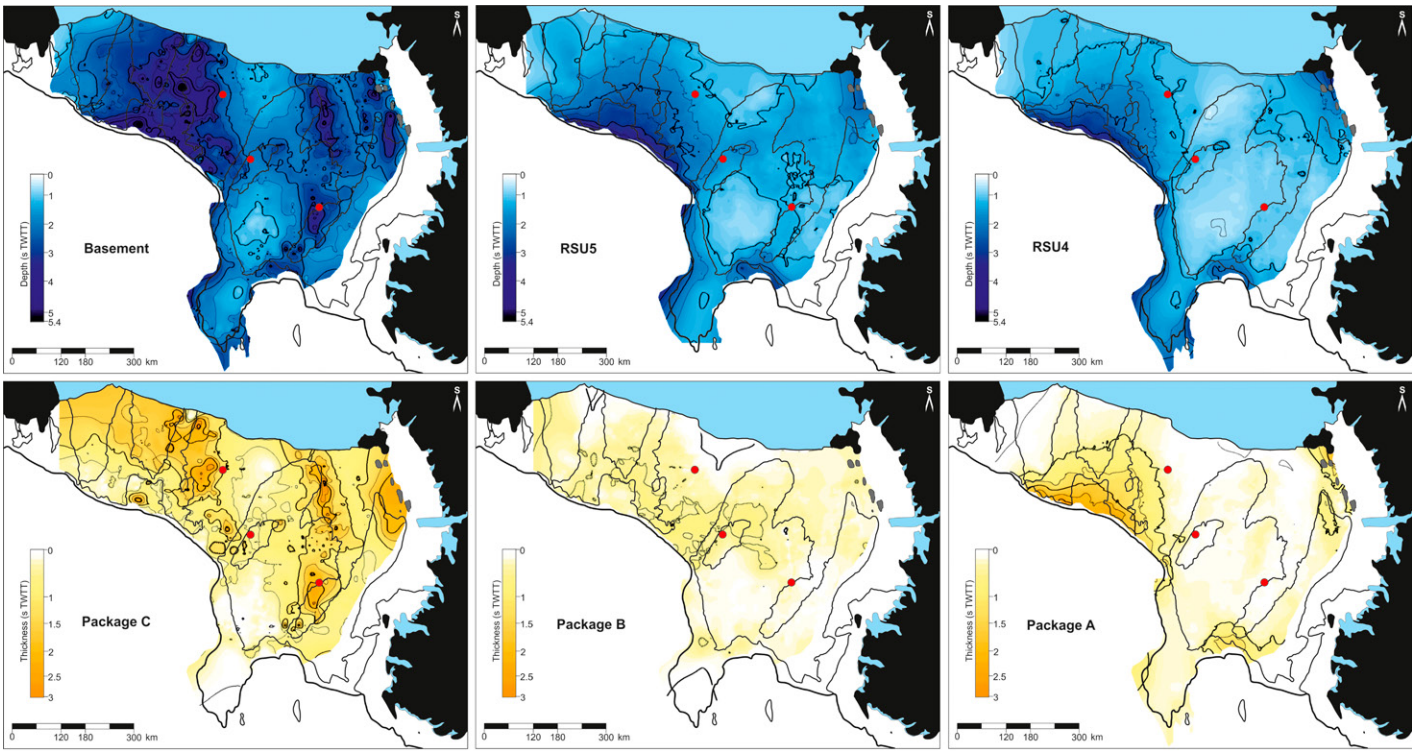

Figure 7. Maps of the Ross Sea continental shelf, Antarctica, and its major interpreted surfaces in depth and seismic packages in thickness both in seconds two-way travel-time (TWTT). Isolines at 0.5 s intervals. Modern continental shelf edge is marked by the thick black line and the thin black lines outline banks and basins as in Figure 1B. The locations of the three considered sites are marked with red dots.

Glomar Challenger Basin and middle shelf of Whales Basin (Fig. 7). The average thickness of Package B in the sedimentary basins is 0.4 s TWTT, but in the Joides Basin the record only exceeds 0.2 s TWTT in the inner part. Conversely, in Glomar Challenger Basin, the depocenters are recorded toward the present-day outer continental shelf. Pennell Basin has the largest thickness of the package in a ~200-km-wide NE-SW zone aligned with the trough in RSU4 surface, where the U1521 drill site is located (Fig. 7).

Major stratigraphic changes in the sedimentary record of Package B define two seismic sequences that present an irregular distribution over the continental shelf of the Ross Sea (Fig. 3B). Further stratigraphic discontinuities can be distinguished in each of the seismic sequences (Fig. 2). A total of four regionally mappable seismic units can be distinguished between RSU4 and RSU5 in Pennell Basin (Fig. 3B). These seismic units distinguish several seismic subunits bounded by minor stratigraphic discontinuities. A detailed description of the seismic units and stratigraphic discontinuities is provided below.

Seismic Unit RSS4-I

RSS4-I has restricted distribution from the westernmost Glomar Challenger Basin, across the Ross Bank, Pennell Basin, and Pennell Bank, to the easternmost Joides Basin (Fig. 9). Its lenticular geometry is the result of its lower boundary being truncated by its upper boundary, the RSU4 surface (Fig. 3). Maximum thickness of RSS4-I (>0.2 s TWTT) occurs to the southwest of IODP Site U1521. Seismic profile PD90_36 shows ~0.10 s TWTT of sediment associated with RSS4-I overlying the recovered interval 9 km to the southeast of Site U1521 (Fig. 3B). Thus, the seismic-stratigraphy indicates that Site U1521 has only captured the lower half of this unit. The amplitude and lateral continuity of the reflections forming RSS4-I decrease downwards in the record (Figs. 2, 3B, and 4). Laterally continuous reflections dip toward the Ross Bank in the eastern margin of Pennell Basin and toward the Pennell Bank in the eastern Joides Basin. They bound low lateral continuity and chaotic reflections (Figs. 2 and 3B).

A relatively gradual increase with depth in the P-wave velocity is registered in RSS4-I at Site U1521 (Fig. 5), while a steeper downwards increase in P-wave velocity is recorded in DSDP Site 273. A sharp decrease in P-wave (1580 to ~1510 m/s) at 130 mbsf in IODP Site U1521 correlates with the change from higher to lower amplitude reflections in the seismic record. Major changes in P-wave values match with the laterally continuous dipping reflections distinguished within this unit (Fig. 4B). The spatial velocity distribution shows local layers with high to very high P-wave values (>2350 m/s) interbedded in the average record of low P-wave values (<2100 m/s) (Fig. 3C).

Low and homogeneous density values characterize RSS4-I in the Pennell and Joides basins, but slightly higher density values are observed at the bottom of the unit in DSDP Site 273 (Fig. 5). At Site U1521, resistivity values and magnetic susceptibility decrease downwards, whereas the natural gamma radiation and the water saturation increase downwards with highly variable values (Fig. 5). FMS images also reveal low resistivity sediments forming this unit.

The bottom of RSS4-I is formed by the stratigraphic discontinuity D-a. Discontinuity D-a constitutes a high lateral continuity reflection that varies from medium to high amplitude. It is largely conformable with the underlying record. D-a represents a local boundary between overlying low reflectivity and underlying high reflectivity seismic facies (Fig. 3B). It is found at 210 mbsf at Site U1521 and at 166 mbsf at DSDP Site 273, corresponding to a sharp increase in P-wave, density, and magnetic susceptibility values (Fig. 5).

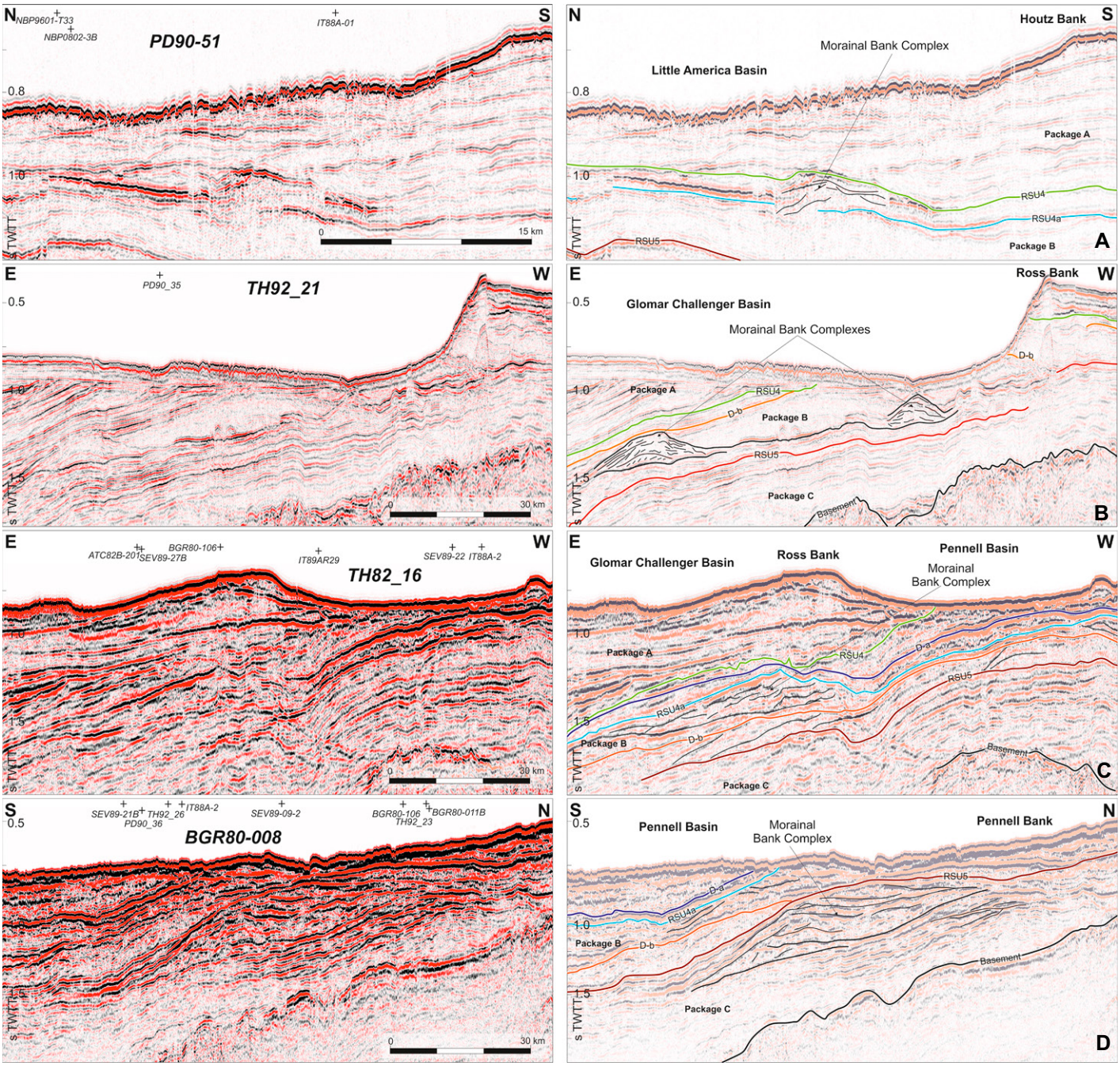

Figure 8. Ross Sea examples of the mounded-elongated bodies interpreted as morainal bank complexes. (A) Little America Basin below RSU4 (in RSS4) in the single channel profile PD90_51. (B) Glomar Challenger Basin below RSU4a (in RSS3-II) in multichannel seismic (MCS) profile TH82_16. (C) Glomar Challenger Basin below D-b (in RSS3-II) in MCS profile TH92_21. (D) Pennell Basin below RSU5 (in Package C) in MCS profile BGR80-008. See locations in Figure 1B (pink lines). TWTT—two-way travel-time. The crossing line points are marked.

Seismic Unit RSS4-II

RSS4-II is locally identified in the basins and banks from Houtz Bank to Joides Basin, but is absent over Iselin Bank (Figs. 3B and 9). It presents a patchy distribution with large areal extension along a NE-SW corridor which extends from the northwest of the Glomar Challenger Basin to the southeast of the Central Basin. The overall thickness of RSS4-II averages ~0.1 s TWTT with local depocenters of >0.2 s TWTT (Fig. 9).

The internal structure of RSS4-II shows variability in both seismic facies and in logged physical properties (Figs. 2 and 4). A minor discontinuity formed by a high amplitude and laterally continuous reflection bounds two seismic subunits, RSS4-IIa and RSS4-IIb (Fig. 2). Seismic Subunit RSS4-IIa, is formed by very high amplitude and laterally continuous reflections. Very low amplitude reflections with little to no lateral continuity form the semi-transparent lower subunit, RSS4-IIb (Fig. 3B). Across the Joides Basin to Ross Bank region, the two subunits appear to represent lateral variations of interrelated

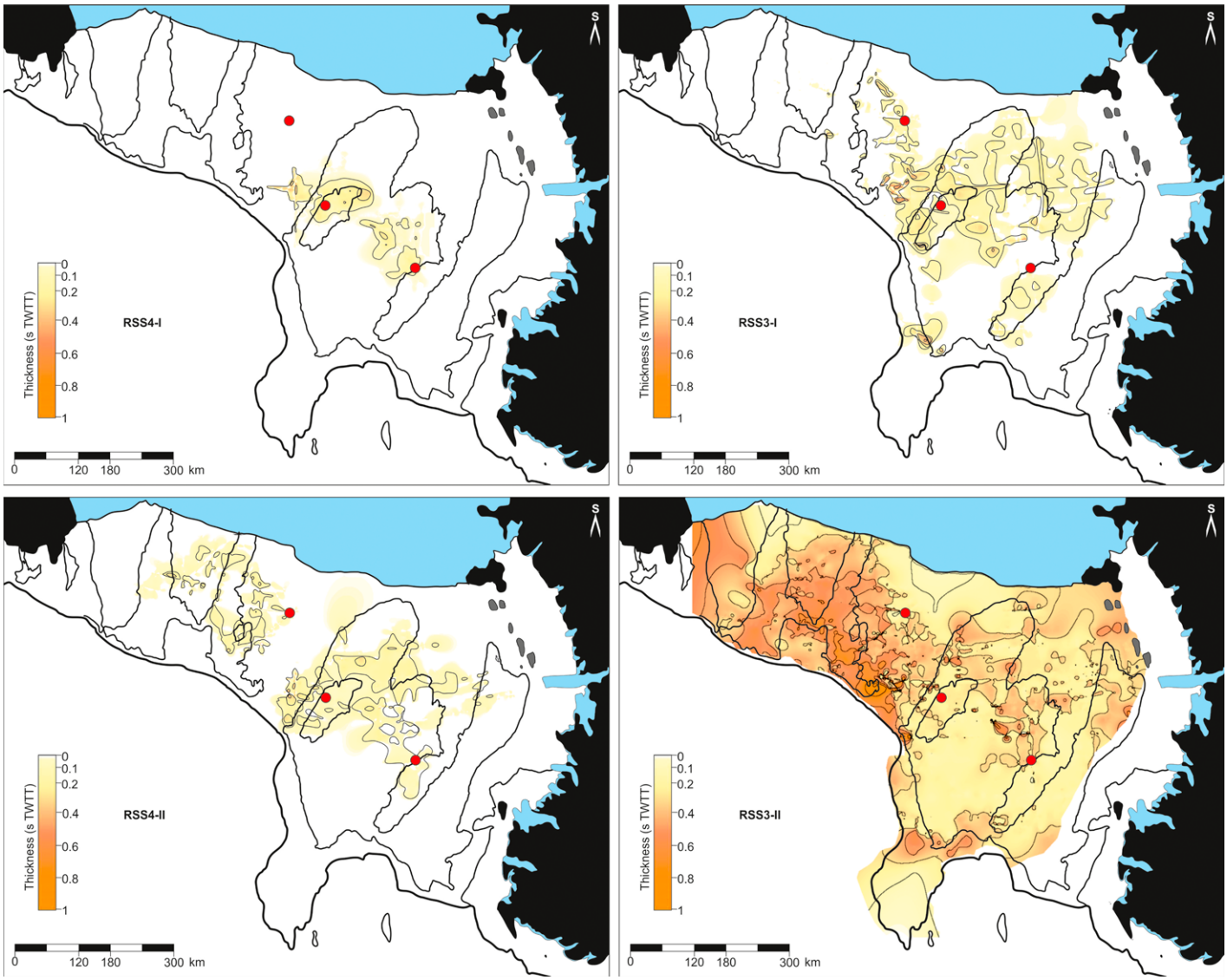

Figure 9. Maps of the Ross Sea continental shelf, Antarctica, showing thickness of individual seismic units in seconds two-way travel-time (TWTT). Isolines at 0.1 s intervals, except in RSS3-II where they are at 0.2 s. Modern continental shelf edge is marked by the thick black line and the thin black lines outline banks and basins as in Figure 1B. The locations of the three considered sites are marked with red dots.

seismic facies. However, in the Whales and Joides basins the seismic facies are more uniform in nature within RSS4-II, and form inclined moderate amplitude reflections that appear to terminate at the underlying RSU4a discontinuity (Figs. 3B and 6). Mounded-elongated bodies with offshore dipping internal reflections are locally identified in Houtz Bank and eastern Glomar Challenger Basin. They are ~0.2 s TWTT thick and 10–20 km long (Fig. 8A).

RSS4-II presents relatively high P-wave values (Fig. 5), particularly in RSS4-IIa (maximum 2500 m/s), with a general downwards decreasing trend. The spatial velocity distribution shows a thick layer of high P-wave values (>2400 m/s) in RSS4-II in the western part of Pennell Basin (Fig. 3C). The density of RSS4-II is relatively high where RSS4-IIa presents higher density values (~1.9 g/cm^3) than RSS4-IIb (~1.7 g/cm^3). The porosity of the unit is generally higher in the Glomar Challenger and Joides basins with respect to Pennell Basin. Resistivity, magnetic susceptibility, and natural gamma radiation increase downwards reaching their maximum around 240 mbsf at Site U1521 with a downwards decreasing trend below. Water saturation shows a downward decreasing trend (Fig. 4).

At the bottom of RSS4-II, the stratigraphic discontinuity RSU4a constitutes a medium to high amplitude reflection. It presents as a laterally continuous reflection forming a sharp truncation surface along the eastern margin of Pennell Basin and in the eastern Joides Basin (Fig. 3B). It locally separates high amplitude reflections above and below, while laterally the underlying record tends to be less reflective than the overlying one (Fig. 3B). RSU4a is located at 200, 288, and 228 mbsf at DSDP Site 272, IODP Site U1521, and DSDP Site 273, respectively (Fig. 5). At the DSDP sites, it represents a change from heterogeneous P-wave and density values above to homogeneous values of both properties below it, but at Site U1521 the change is reversed (Fig. 4).

Seismic Unit RSS3-I

Below RSU4a, RSS3-I is identified in the westernmost Glomar Challenger Basin. It is broadly distributed across the Pennell and Joides basins (Fig. 9). The thickest sections are recorded in the western part of Glomar Challenger Basin and the southeastern part of Pennell Basin,

as well as the central area of the Pennell Bank, where depocenters over 0.25 s TWTT are locally identified (Fig. 3B). However, the Joides Basin displays comparatively thinner intervals with values only locally reaching 0.1 s TWTT (Fig. 9).

RSS3-I is divided into two subunits, with Seismic Subunit RSS3-Ia containing high amplitude reflections that are laterally continuous in the upper part of the unit, and a lower Seismic Subunit RSS3-Ib that contains discontinuous to chaotic reflections (Figs. 2 and 3B). In the Pennell Basin, the base of RSS3-Ia goes down to 1.15 s TWTT, which corresponds to 339 mbsf, at Site U1521, but the unit pinches out laterally toward RSU4a (Fig. 3B). In the MCS profiles, RSS3-Ia is mainly composed of two reflections of very high amplitude, the upper one of which exhibits the same polarity as the seafloor reflection (Supplemental Fig. S3). RSS3-Ia occurs widely along the southeastern part of Pennell Basin and toward Ross Bank over an area of more than 5000 km^2. At IODP Site U1521, it has a thickness of 65 m (0.055 s TWTT), but reaches maximum thicknesses >0.07 s TWTT within the Pennell Basin, i.e., up to 83 m thick considering the time-depth relation of Site U1521. Along the margin of Pennell Basin with Pennell Bank, RSS3-Ib is formed by layers of chaotic to low lateral continuity reflections that locally form mound morphologies. They are bounded by high amplitude reflections which exhibit rough morphology (Fig. 3B). Mounded-elongated bodies have been identified along the northern Whales Basin, the eastern margin of the Glomar Challenger Basin, and between the Ross and Pennell banks. They are formed by relatively continuous reflections tilted offshore which form ~0.24 s TWTT thick mounds thinning laterally over ~5 km (Fig. 8C).

P-wave values are relatively constant along RSS3-I in the Glomar Challenger and Joides basins. Only the highly variable ranges of P-wave velocity (2100–2700 m/s) in Pennell Basin show a general downward decreasing trend (Fig. 5). At Site U1521 downhole logs of P-wave velocity associated with RSS3-Ia display wide variations up to a maximum value of 4300 m/s. The average is 2500 m/s, with 2300 m/s median and 2100 m/s mode. Overall, the baseline of the velocity increases downwards. In the 2-D velocity distribution, RSS3-Ia shows as a layer of high P-wave values (~2400 m/s) in Pennell Basin (Fig. 3C). Several layers of high P-wave (<2500 m/s) are distinguished in RSS3-I along the Pennell Basin and Pennell Bank (Fig. 3C).

The density of RSS3-I averages ~1.6 g/cm^3. However, it shows a general downwards increasing trend within a wide range of values (Fig. 5). The density of RSS3-Ia is relatively high with an average of ~1.7 g/cm^3 with downwards increasing trend. The major change in density occurs at the bottom of RSS3-Ia (Fig. 4). RSS3-I presents low porosity at Site U1521, which increases from ~30% in RSS3-Ia to ~40% in RSS3-Ib. On the contrary, high porosity values are calculated at DSDP sites 272 and 273 (Fig. 5). The acoustic impedance of RSS3-Ia shows a sharp change from the overlying sediments. Its values range from 2.7×10^6 to 3.8×10^6 kg/m^2 s with two distinct maximum values at the top and medium parts of the subunit. Resistivity values oscillate in a wide range in RSS3-I. Maximum values (8.7 Ohm·m) are recorded in the upper part of the unit matching with RSS3-Ia, as the highest resistivity of the stratigraphic column (Fig. 5). The FMS images show an alternating pattern of conductive and resistive layers in RSS3-Ia, whereas homogeneously conductive sediments are identified in RSS3-Ib. Natural gamma radiation and water saturation values increase downwards, in contrast to the trend in magnetic susceptibility, which has higher values at the top of RSS3-Ia and in RSS3-Ib (Fig. 5).

At the bottom of RSS3-I, the stratigraphic discontinuity D-b shows as a medium to high amplitude, laterally continuous reflection that can be correlated regionally (Fig. 3B). It is generally overlying low reflectivity seismic facies. At DSDP Site 272, IODP Site U1521, and DSDP Site 273, it is placed at 278, 385, and 235 mbsf respectively (Fig. 5). D-b overlies a relatively homogeneous P-wave values record, compared with the wide range values in RSS3-I (Fig. 4).

Seismic Unit RSS3-II

Below D-b, RSS3-II occurs over a wide area and is thickest in the eastern Ross Sea. Depocenters exceeding 0.6 s TWTT are elongated along the outer Hayes Bank and Glomar Challenger Basin (Fig. 9). RSS3-II is formed by reflections with low amplitude and little to no lateral continuity, bounded by low amplitude and laterally continuous reflections that form minor stratigraphic discontinuities (Fig. 2). The patterns formed by these seismic facies form up to 0.24 s TWTT thick prograding wedges which generally dip toward the central part of the basins (Figs. 3, 6, and 10). In addition, mounded-elongated bodies have been identified in the southwest margin of Glomar Challenger Basin (Fig. 8B). These mounded bodies are ~0.15 s TWTT thick and ~22 km long. They are formed by relatively continuous reflections tilted toward the central part of the basin. Similar mounded-elongated bodies are locally identified in Pennell Basin and Ross Bank.

P-wave values in RSS3-II oscillate within a limited range showing a downward increasing trend in Joides Basin (Figs. 4 and 5). The minor discontinuities match with marked changes in the P-wave velocity. The spatial velocity distribution shows a few layers of high P-wave (<2500 m/s) dipping toward the central edge in the eastern side of Pennell Basin (Fig. 3C).

The overall density of RSS3-II is relatively low with a general trend of slightly downwards decrease (Fig. 5). RSS3-II presents low porosity in Pennell Basin (38%) and high porosity in the Glomar Challenger and Joides basins (up to 85%). Resistivity, natural gamma radiation, and magnetic susceptibility are constant in the upper part of the unit, whereas they increase from 511 mbsf downwards at Site U1521. The water saturation in RSS3-II increases downwards to ~530 mbsf, decreasing to the bottom of the unit in Pennell Basin (Fig. 5).

Discontinuity RSU5 forms the bottom boundary of RSS3-II and the Seismic Package B, and is identified as a high amplitude and laterally continuous reflection that is generally conformable with the underlying record (Figs. 3A and 6). Local truncation of the underlying record is visible on the seismic sections of the eastern margin of Little America Basin and the northern margin of Glomar Challenger Basin. RSU5 is regionally identified at the top of high reflectivity and stratified deposits. Sparse mounded-elongated bodies locally underly RSU5 (Fig. 8D). RSU5 is identified at 341, 566, and 282 mbsf at DSDP Site 272, IODP Site U1521, and DSDP Site 273, respectively, and represents a sharp increase in P-wave, density, and acoustic impedance toward the underlying record (Figs. 4 and 5). Regionally, RSU5 is located around 2 s TWTT deep in the eastern Ross Sea, whereas the average depth is 1.2 s TWTT in the western Ross Sea. Maximum depths (>3 s TWTT) are reached along the shelf edge of the Houtz and Hayes banks and Whales Basin. Minimum depths (<0.8 s TWTT) are in the inner part of Glomar Challenger Basin, landwards of Iselin Bank in Pennell Bank and the middle shelf of Joides Basin and Crary-Mawson Bank (Fig. 7).

UNIFYING DRILL CORE LITHOSTRATIGRAPHIES FOR SEISMIC STRATIGRAPHIC CORRELATION

The core-log-seismic tie allows correlation of the main lithological components of the distinguished seismic sequences, units, and subunits (Fig. 4). However, due to the use of different descriptive techniques and lithological classification schemes, the existing lithological descriptions from DSDP Leg 28 cores are inconsistent with the IODP Expedition 374 core descriptions. Here, we apply the lithological classification scheme from IODP Expedition 374 (McKay

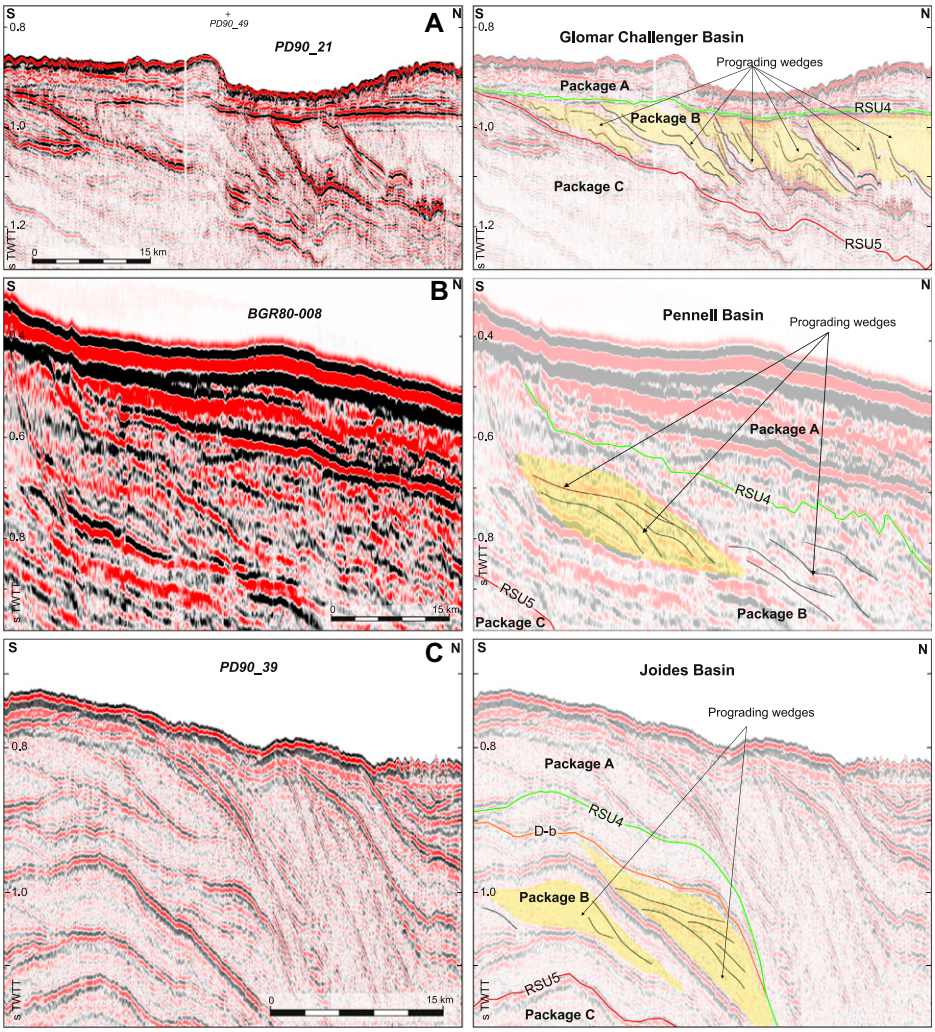

Figure 10. Seismic profile fragments in the Ross Sea showing prograding wedges in RSS3-II (Package B). (A) Inner continental shelf of Glomar Challenger Basin, single channel seismic (SCS) profile PD90_21. (B) Middle continental shelf of Pennell Basin, multi-channel profile BGR80-008. (C) Outer continental shelf of Joides Basin, SCS profile PD90_39. See location in Figure 1B (green lines). TWTT—two-way travel-time. The crossing line points are marked.

et al., 2019) to the DSDP sites 272 and 273. In this study, we use the quantitative grain size analysis conducted by Balshaw (1981) to reclassify the major lithostratigraphic units for DSDP sites 272 and 273 presented in Hayes et al. (1975).

For DSDP Site 272, the upper 121 mbsf were previously described as diatom-bearing silty clay containing common clasts. However, <10% diatoms and >25% sand content (reaching 50% in places) conforms to the diamictite classification of IODP Expedition 374 (Fig. 4A). Below 121 mbsf, sand content drops below 25%, and gradually decreases downcore to values generally <10% by ~148 mbsf (Balshaw, 1981). Coincident with this decrease in sand is an increase in diatom content. The lithology can be classified as diatom-rich mudstone between 137 and 175 mbsf, and as mud-bearing diatom oozes below 175 mbsf. Clasts become rare to absent in the diatom ooze layers, and bivalves are noted (Hayes et al., 1975; Balshaw, 1981; Dell and Fleming., 1975). Between 365 and 441 mbsf (base of site), the core consists of lithified mudstone, some of which is either silica or carbonate cemented (Hayes et al., 1975).

At DSDP Site 273, the upper 26 mbsf was described as a pebbly silty clay by Hayes et al. (1975) but contains >25% sand, so is reclassified here as diamictite (Fig. 4C). Below 26 mbsf most of the core was described as silty clay with pebbles, some of which is diatom-bearing. However, only a short interval between ~139 and 150 mbsf contains 10–40% diatoms and is classified as diatom-rich mudstone with clasts. Sand content between 26 and 272 mbsf generally varies between 15% and 20%, and is classified as mudstone (Fig. 4C). Grainsize indicates the presence of diamictites in two short intervals at 136 and 215 mbsf. The 215 mbsf interval was described as "gritty-looking," silty clays with pebbles by Hayes et al. (1975). Below 272 mbsf, the sand content increases from 21% to 30%, indicating a downcore coarsening reflecting a shift toward sediments that are either diamictites or close to the classification threshold of 25% sand. Carbonate cement is also noted in intervals below 272 mbsf (Hayes et al., 1975).

Consequently, Package A corresponds to diamictites at DSDP Site 272 (Glomar Challenger Basin) and DSDP Site 273 (Joides Basin). The Package A lithostratigraphy in Pennell Basin is dominated by diamictites interbedded with thin, highly-deformed diatom oozes (Fig. 4), that characterize lithostratigraphic units I and II at Site U1521 (McKay et al., 2019).

Package B at DSDP Site 272 (Glomar Challenger Basin) is characterized by 16 m of diatom-bearing mudstone, overlying diatom ooze with low clast abundance (30–70%), and some shell fragments (Fig. 4A) (Hayes et al., 1975; Balshaw, 1981). In Pennell Basin (IODP Site U1521), Package B consists of bioturbated diatom-bearing/rich mudstone with bivalves and rare clasts in Lithostratigraphic Unit III (McKay et al., 2019), forming the upper part of the sequence that constitutes the interpreted Seismic Unit RSS4-I. Below this, interbedded mudstone and diatom-bearing, clast-poor, sandy diamictites form Lithostratigraphic Unit IV (McKay et al., 2019), correlating to Seismic Unit RSS4-II (Fig. 4B). Seismic Subunit RSS3-Ia correlates with Lithostratigraphic Unit V (McKay et al., 2019), which consists of chert nodules and silica cemented mudstone with rare clasts. Seismic Subunit RSS3-Ib is formed by the massive diamictite with silica-cemented mudstones of Lithostratigraphic Unit VIA (Fig. 4B). Seismic Unit RSS3-II correlates with Lithostratigraphic Unit VIB, consisting of a 60.5-m-thick interval of cemented diamictite, and Lithostratigraphic Unit VIC, consisting of a 127-m-thick interval dominated by cemented diamictite but with thin cm- to m-scale bioturbated mudstone beds (McKay et al., 2019). At DSDP Site 273 in Joides Basin, Package B corresponds to mudstones with variable clast contents ranging from abundant to sparse, and comparatively thin (~11 m) intervals of diatom-rich mudstones (Fig. 4C) (Hayes et al., 1975).

The recovered Package C consists of silica cemented mudstones with rare clasts at DSDP Site 272 in the Glomar Challenger Basin (Hayes et al., 1975), while in the Pennell Basin the record is dominated by diamictite with carbonate concretions and occasional thin intervals of fine wavy mudstone laminations (Fig. 4), i.e.,

Lithostratigraphic Unit VII at IODP Site U1521 (McKay et al., 2019). At DSDP Site 273 in the Joides Basin, the mudstones with clasts forming the lower package have a higher sand content than the unit above (20–25%), and are classified as diamictites (>25%) in some intervals (Fig. 4). This section also shows an increase in lithification and contains carbonate cemented intervals (Hayes et al., 1975; Balshaw, 1981).

AGE CORRELATION

The ages of the main stratigraphic discontinuities, seismic sequences, and units are estimated in this work on the basis of the preliminary shipboard age model of IODP Expedition 374 (McKay et al., 2019), and a revision of the DSDP sites biostratigraphy conducted by Tuzzi (2009) (Table 2). The upgraded age estimates on the DSDP sites are in general older than previously published (Table 2), i.e., sediments older than ca. 15.8 Ma occupy DSDP Site 272 below ~150 mbsf; and DSDP Site 273 recovered sediments between >16.2 Ma and ca. 18 Ma below ~34 mbsf. The most recent chronostratigraphies obtained during IODP Expedition 374 are still a work in progress (McKay et al., 2019), but the seismic-stratigraphic ties provided here will give insights into the final age models through identification of missing stratigraphic sections and distinct chronostratigraphic horizons at each site.

Broadly, the ages of Package A, Package B, and Package C that were sampled by cores presented in this work correspond to mid-Miocene to Pleistocene (ca. 14.6 Ma to present), early to middle Miocene (ca. 18–14.6 Ma), and early Miocene and older (>18 Ma), respectively. During the early to middle Miocene period, the detailed seismic-stratigraphy in Package B constrained by DSDP sites 272 and 273 and IODP Site U1521 allows us to distinguish seismic units and subunits which are related to ice sheet variation prior to, during, and after the MCO.

DIAGENETIC OPAL FRONT

Within the regional seismic facies of RSS3-I, RSS3-Ia forms a clearly mappable subunit across the Pennell Basin and Pennell Bank (Fig. 3B). It is formed by very high amplitude reflections that result in a distinct high-velocity layer in the 2-D velocity distribution (Fig. 3C). At a broader scale, the reflection tomography on line IT94AR126 shows a sharp downwards increase in P-wave velocity within Package B correlating with the stratigraphic level of RSS3-Ia (from <1700 m/s to >2500 m/s; Supplemental Fig. S3). The outstanding character of RSS3-Ia is related to the silica cemented mudstones and chert revealed in the lithology, and the above average Si/Ti ratios in cores recovered at Site U1521 (McKay et al., 2019). The opal content of RSS3-Ia is inferred to be related to the diagenetic alteration of diatom-bearing mudstone and diatom oozes, which were deposited sometime between ca. 17.4 and 16.9 Ma (Table 2), prior to the event that resulted in RSU4a.

The shipboard work during IODP Expedition 374 has revealed that the diatom content of RSS3-Ia (Lithological Unit III) has undergone opal-A (amorphous) to opal-CT (cristobalite-tridymite) diagenesis (McKay et al., 2019). As a result of the opal A/CT front, RSS3-Ia shows extreme values for most of the physical properties and the formation of high-velocity layers (Figs. 3C, 4B, and 5C). Anomalous values of key physical properties are commonly identified in opal A/CT diagenetic fronts forming chert levels (e.g., Nobes et al., 1992; Neagu, 2011). A sharp decrease in porosity matches with an increase in density in RSS3-Ia with respect to the overlying sediment (Fig. 5C). The transformation of opal-A to opal-CT in silica-rich sediment may reduce porosity by over 30% (e.g., Isaacs, 1981; Tada, 1991). In addition, extremely high resistivity values are recorded at the top of RSS3-Ia along with variation between high and very high values, which probably reflects the regional heterogeneity of the diagenetic front (Fig. 5C). This heterogeneity is revealed by FMS images that show thin layers of extremely high resistivity, interbedded with thin layers of very high conductivity, and suggests that RSS3-Ia is characterized by distinct layers of chert interbedded with opal-A that has not undergone diagenetic conversion and/or terrigenous sediments. Following the resistivity trend, the natural gamma radiation values in RSS3-Ia are equally high (Fig. 5C), reflecting increases in Th and K (McKay et al., 2019). Sharp increase of resistivity and Th and K concentration estimates from the downhole natural gamma radiation measurements are a common signature of silica diagenetic fronts (Nobes et al., 1992).

The sharp change in velocity and density results in a very high acoustic impedance contrast, causing the high amplitude reflections forming RSU4a and the underlying RSS3-Ia in the seismic record (Figs. 3, 4B, and 5C). The seismic data reflect therefore the occurrence of an opal front and allow us to infer the basin-wide scale of this transition. The contrast in acoustic impedance would usually result in a bottom simulating reflector (BSR) crosscutting stratigraphic reflections, as widely reported from other areas in which biosiliceous sediments occur (e.g., Hein et al., 1978; Lonsdale, 1990; Bohrmann et al., 1992; Tribble et al., 1992; Davies and Cartwright, 2002). The BSR would mimic the seafloor morphology at the time of the diagenetic front formation (e.g., Bohrmann et al., 1992; Davies and Cartwright, 2002). This front migrates upwards in the stratigraphic column as sediments accumulate. The implications of the depth occurrence of RSS3-Ia is extensively discussed in the Supplemental Material.

The diagenetic transition could have resulted from a thicker-than-present sedimentary cover over RSU4a. The extensive erosion that occurred during the formation of discontinuity RSU4 in the Pennell Basin and Ross Bank (Figs. 3B and 11) could be linked to the loss of significant amount of sediments previously placed over the diagenetic front. In this case, the high diatom content of RSS3-Ia went through the opal A/CT diagenetic front due to an overlying thick sediment cover. We infer that the formerly overlying sediments were subsequently removed during RSU4 formation and repetitive late Miocene to Pleistocene ice advance over Pennell Basin (see Package A discussion below). The original morphology of RSS3-Ia could be related to the shape of the overlying sediment cover during the active transformation of opal-A to opal-CT. In chert layers forming BSRs, the degree of conformity between the chert reflection and the host stratigraphy has been used to estimate the timing

TABLE 2. ESTIMATED AGES OF THE MAIN STRATIGRAPHIC DISCONTINUITIES IN THE ROSS SEA BASED ON THE AGE OF THE SEDIMENTS ABOVE AND BELOW THE DISCONTINUITIES ACCORDING TO PREVIOUSLY PUBLISHED AGE MODELS

Site reference: Discontinuity	U1521 McKay et al. (2019)	DSDP272 updated	DSDP272 Tuzzi (2009)	DSDP273 updated	DSDP273 Bart (2003)	DSDP273 Tuzzi (2009)	DSDP273 + DSDP272 DeSantis et al. (1995)
RSU4	**14.6**–15.8	>14.3	<15.3–15.8	>16.2	14.4–15.7	<15.5	14.2–16.2
D-a	***~16.7***		–		>14.4	15.5–16.2	>14.2
RSU4a	***~17/16.9***		>15.8		>14.4	16.2–17	17.5
D-b	***~17.4***		15.8–18.1		>14.4	16.77–17	>14.7
RSU5	**~18**	18.1–18.7	<18.1–18.7	~18	>15.7	>17	21

Notes: Ages considered more accurate for the purpose of this work according to latest age models are highlighted in bold. IODP—International Ocean Discovery Program.

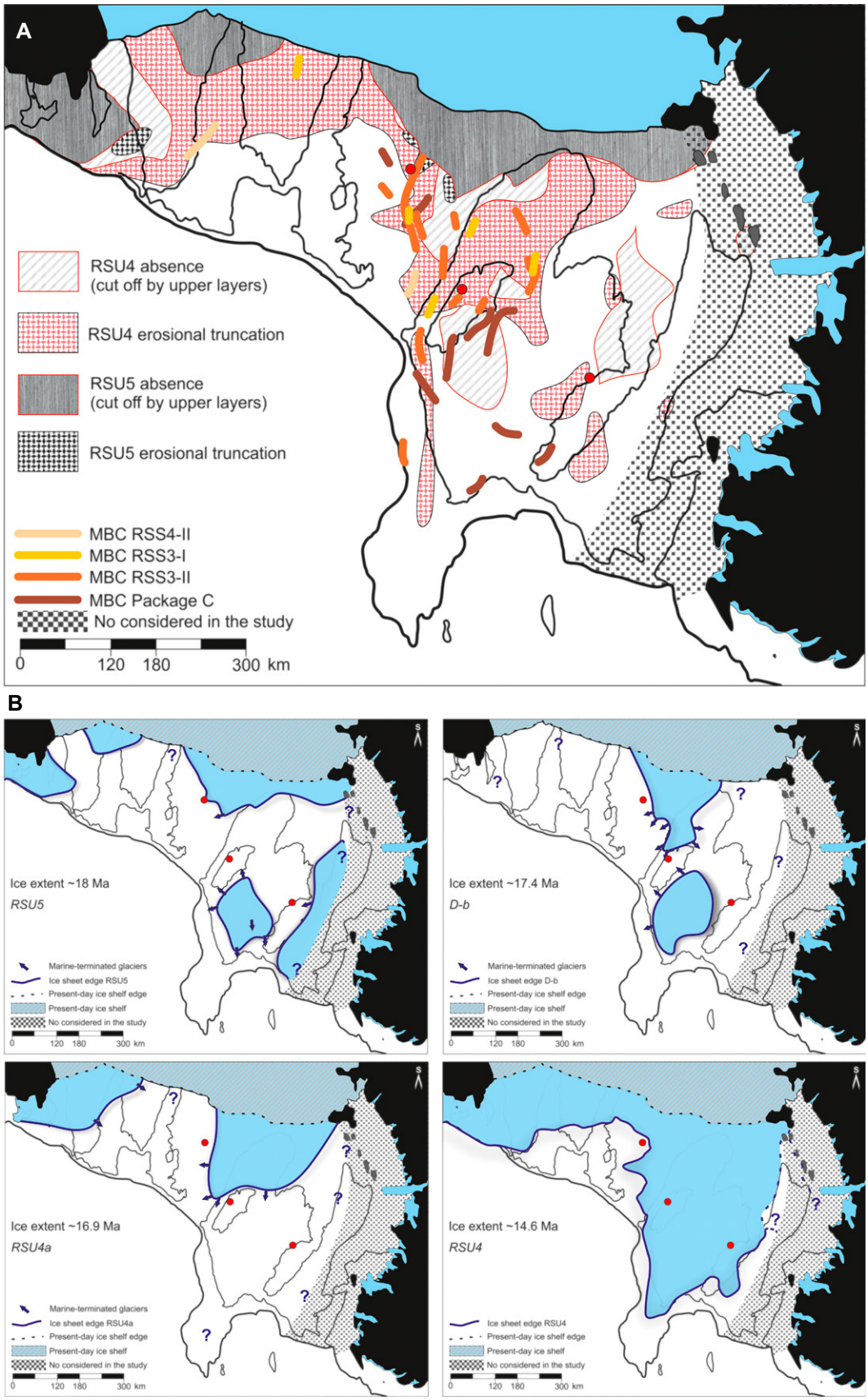

Figure 11. (A) Regional map of the continental shelf of the Ross Sea, Antarctica, showing the extent of erosion on RSU4 and RSU5 and the location of the morainal bank complexes (MBC) identified in the interpreted seismic units. The locations of the three considered sites are marked with red dots. (B) Reconstructions of the tentative most oceanwards extent of the grounded ice edge and marine terminating glaciers during periods of the ice advance from early to middle Miocene based on the depth and sediment distribution maps in Figures 7 and 9, and the features represented in A. The westernmost part of the Ross Sea is out of the scope of this study.

of fossilization of the diagenetic front (Neagu, 2011). However, RSS3-Ia only mimics the morphology of strata directly overlying it (Figs. 3A and 3B). This may be due to the combination of diatom-poor sediments accumulated just above RSU4a, and oscillating ice sheets, particularly above RSU4, that would have altered the paleoseafloor morphology since the time of the diagenetic front formation.

ICE SHEET EXPANSION VS. OPEN MARINE CONDITIONS ON THE ROSS SEA CONTINENTAL SHELF

The continental shelf edge in the Ross Sea has prograded 200–240 km northward in the Glomar Challenger Basin from the Eocene/Oligocene boundary (34 Ma) to present-day (Wilson et al., 2012; Colleoni et al., 2018; Hochmuth and Gohl, 2019). Sediments recovered at Site U1522 during IODP Expedition 374 (McKay et al., 2019) indicate that the post-RSU4 (mid-Miocene to present) continental shelf progradation in the Glomar Challenger Basin has occurred largely due to siliciclastic sediment supply. This is in agreement with the relationship of density and compressional velocity logs of the three sites studied in this work, and the increased natural gamma radiation values within Package A at IODP Site U1521 (Figs. 4 and 5).

Discrete intervals of predominately biogenic sedimentation during the early and middle Miocene are revealed from Site U1521 lithological descriptions (McKay et al., 2019). Diatom-rich muds of Lithostratigraphic Unit III correspond to low density and velocity intervals (Fig. 4B). When such facies are diagenetically altered to silica cemented muds and cherts they present highly variable velocity and density profiles in site logs, including the highest velocity values in the cored section in Lithostratigraphic Unit V (Figs. 4B and 5C). The high-velocity intervals of the chert can be correlated for several tens of kilometers across the seismic grid.

The variety of seismic features identified in this work points to heterogeneous sediment supply during the early to middle Miocene. In addition, migration of depocenters indicates changes of the sedimentary source. Widespread prograding wedges across the sedimentary basins of the Ross Sea continental shelf are interpreted to result from the input of sediments from an ice sheet or ice cap (Fig. 10) (e.g., De Santis et al., 1995; Shipp et al., 1999; Bart and De Santis, 2012). The identified mounded-elongated bodies present a geometry and internal structure commonly related to submarine morainal bank complexes formed by marine-terminating glaciers (Fig. 8) (Powell and Cooper, 2002; Lønne and Nemec, 2011; Dowdeswell et al., 2015). Marine-terminating glaciers rapidly discharge sediment at the grounding line to form morainal bank complexes and fan systems. Considering the spatial and temporal variations in the glacial history of the Ross Sea continental shelf, we discuss three major stages during its Miocene evolution.

Early Miocene (>18 Ma): Open Marine to Ice-Proximal Conditions

Underlying RSU5 (ca. 18 Ma), the uppermost part of Package C has been revised in this study based on the drilling data from DSDP Site 272, IODP Site U1521, and DSDP Site 273 (Supplemental Material). This record contains a stratified aggradational pattern of sedimentation (Figs. 3A, 3B, and 6), and was deposited during a period when the combination of existing morphology, subsidence, and sea level rise created enough accommodation space for the sediments to be deposited and preserved during the early Miocene (Leckie and Webb, 1983). The generally low porosity values of the Package C in Glomar Challenger, Pennell, and Joides basins likely reflect lithification triggered by the overlying sedimentary load (Fig. 5). Lithological descriptions of massive to stratified diamictites (DSDP Site 273 and IODP Site U1521) and lithified mudstones with intervals of cemented silica (DSDP Site 272) are consistent with deposition of the upper part of Package C during general glacimarine environmental conditions, with no clear evidence of grounded ice in the Glomar Challenger Basin from seismic data. The inclined bedding and offshore thickening of strata observed in the seismic lines crossing DSDP Site 272 indicates that this region formed the paleo-continental slope during the early-middle Miocene, prior to RSU4. The deposition of silica cemented mudstone at DSDP Site 272 below RSU5, and diatom-bearing muds and diatom oozes between RSU5 and RSU4 indicates high productivity along the paleo-continental slope existed through most of the early Miocene (Fig. 4A). The sparse submarine morainal bank complexes locally buried below RSU5 along the margins of Pennell and Joides basins are associated with sediment delivery near the ice grounding zone which would have originated from ice caps flowing on local bathymetric highs, some of which may have been subaerial in the late Oligocene to early Miocene (e.g., De Santis et al., 1995, 1999). In the eastern Ross Sea, Package C is thicker along the inner continental shelf, and less sediments accumulated on the outer shelf during this period (Fig. 7). This sedimentary distribution points to a sediment input coming from the south. Thus, the glacial input was absent or constrained to inshore areas in the eastern Ross Sea, generating the proximal depocenters (Fig. 7).

Early to Middle Miocene (18–14.6 Ma): Alternating Glacial to Open Marine Conditions

The eastern Ross Sea depocenters migrated oceanward during the deposition of Package B (Fig. 7). Consequently, Glomar Challenger Basin holds the thickest sedimentary record (<1.2 s TWTT) along its northeastern margin (Fig. 7). Absence of sediment to the south is consistent with missing strata and condensed sequences near the present-day Ross Ice Shelf front (Figs. 6 and 11). RSU4 constitutes a major erosional surface along the southwestern Ross Sea (Figs. 3C, 6B, 10A, 10B, and 11). The increasing velocity toward the outer shelf in Package B revealed by the broad seismic tomography model (Supplemental Fig. S3) may reflect major sediment compaction due to the sediment load, as the sedimentary depocenter shifted further offshore due to continental shelf progradation driven by inland erosion during periods of glacial expansion in West Antarctica. Assuming the timing of bounding unconformities RSU5 and RSU4 is similar across the basins, the similar thicknesses of Package B within the depocenters of the Pennell and the Glomar Challenger basins suggests similar rates of sedimentary input to both basins during the latest early and middle Miocene. The source region of these depocenters potentially varies for each basin according to the location and morphology of the found prograding wedges (Figs. 3, 6, and 10). One caveat here is that the RSU4 erosional events may have removed the upper part of the Package B interval in distinct parts of these basins, particularly inland from the main depocenters (Figs. 7 and 11).

Sharp changes in the physical property baselines above RSU5 at Site U1521 with respect to the values below, particularly magnetic susceptibility values (Fig. 5C), may reveal input of terrigenous material from different sources. Located on the inner continental shelf, drill Site AND-2A contains four well-dated hiatuses, interpreted as periods of maximum ice advance. Three of them, dated at 13.7–14.4 Ma (U4), 14.6–15.9 Ma (U3), and 18–18.7 Ma (U2), overlap with the stratigraphic record recovered at IODP Site U1521, and are interpreted to represent expansion of grounded marine-based ice sheet well beyond the AND-2A Site (Passchier et al., 2011; Levy et al., 2016). Using the preliminary age model of Site U1521 (Table 2), the U2 unconformity coincides with the inferred timing of RSU5 as mapped in this work, whereas U3 and U4 correlate with RSU4. The influence of ice sheet dynamics on the Ross Sea sedimentary basins during the early and middle Miocene is further discussed below.

RSU5 to D-b (RSS3-II): Onset of Progradation and Regional Ice Expansion

The widespread prograding wedges forming the depocenters of RSS3-II point to widespread glacimarine to subglacial environment in the Ross Sea continental shelf (Figs. 3B, 6, and 10). In Pennell Basin, current age constraints at IODP Site U1521 suggest that the ~200 m of poorly sorted glacimarine sediments (diamictites with thin mudstone beds) associated with RSS3-II were emplaced within approximately half a million years (McKay et al., 2019). The RSS3-II sediment thickness is even more extensive in the Glomar Challenger Basin, which is characterized by finer-grained and diatom-rich mudstones and oozes at DSDP Site 272. As it was located on the paleo-continental slope, the site was not under direct subglacial influence (Fig. 3B). The differences in the sedimentary record geometry and thicknesses in the various Ross Sea basins are attributed here to heterogeneous ice flow and sediment delivered from ice caps situated on the local bathymetric highs as well as ice sheets growing from East and West Antarctica. Some of the bathymetric highs of the present-day continental shelf could have been emerged (Paxman et al., 2019), thus nucleating localized ice caps. Alternatively, floating ice shelves could have formed ice rises when making contact with bathymetric highs as described in the Weddell Sea (Larter et al., 2012; Lavoie et al., 2015). The generalized ice advance is interpreted to have led to the widespread deposition of prograding sediment wedges in the southern Glomar Challenger, Pennell, and Joides basins (Figs. 8 and 10). The sparse submarine morainal bank complexes along the southwest margin of Glomar Challenger Basin and the eastern margin of the Ross Bank in RSS3-II occur in the same unit as the prograding wedges (Figs. 8B and 11). This suggests the marine-terminating glaciers responsible for depositing the morainal banks were also associated with voluminous discharge of turbid subglacial meltwater accounting for the sediment delivery of the prograding wedges. Thus, subglacial/ice-proximal conditions occurred in the southern part of the Glomar Challenger Basin and the Ross Bank, in the vicinity of the modern Ross Ice Shelf calving line, from ca. 18 to ca. 17.4 Ma. Further offshore, at DSDP Site 273, this interval is poorly recorded, suggesting that either loading by inland ice or refocusing of sediments by the expanded ice sheet led to a shift in the sedimentation.

D-b to RSU4a (RSS3-I): Chertified Layers and Ice Retreat

The broad range of seismic facies of RSS3-I across basins and banks suggest changing regional environmental conditions between ca. 17.4 Ma and ca. 16.9 Ma within the Ross Sea (Fig. 3). The margins of Pennell Basin are characterized by alternating erosional surfaces and chaotic facies forming several subunits within RSS3-Ib (Fig. 3A). A similar alternating pattern has been observed in a meltwater rich environment (e.g., Kehew et al., 2012), as well as the inferred episodic glacial advance over Sabrina Coast, in East Antarctica, during late Eocene to late Miocene (Gulick et al., 2017). The rough morphology of the high amplitude erosional surfaces points to strong bottom currents, potentially related to outwash or sub-ice cavity, discontinuous meltwater release. The interbedded chaotic facies were delivered from ice-proximal sedimentation during episodic ice sheet/cap retreat. The ice-proximal to distal glacimarine origin of the sediments in the Pennell Basin would be consistent with the low velocity of Pennell Basin and Ross Bank sediments in the tomography model (Supplemental Fig. S3). At the AND-2 Site, the EAIS is interpreted to have retreated from marine-based margins from ca. 17.4 Ma, to a terrestrial terminating system by ca. 16.9 Ma, and advances beyond the Victoria Land Coast were more restricted after this time. In the southern Pennell Bank, glacimarine sedimentation is consistent with proximal ice grounding up to ca. 17 Ma, followed by distal deposition of diatom-rich sediments after this time. This regional ice retreat in the Ross Sea correlates with a eustatic sea-level highstand between 17.3 and 16.6 Ma (Kominz et al., 2016; Levy et al., 2019). Marine-terminating glaciers feeding the morainal bank complexes of this unit across the inner continental shelf (Figs. 8C and 11) would have still advanced from the ice margin likely retreated to the south during most of the sedimentation of RSS3-I.

The chert level identified in RSS3-Ia proves to be highly heterogeneous across the Pennell Basin, suggesting that the original diatom deposition was concentrated into distinct regions (Figs. 5 and 9). This is consistent with deposition of modern diatom-rich sediments around Antarctica's margin, where diatoms remain in suspension even under low oceanographic current regimes and are consequently advected and accumulate in bathymetric depressions (Dunbar et al., 1985; Prothro et al., 2018). The FMS images show a high frequency cyclicity in the deposit of the chert layers in RSS3-Ia, which could relate to climate forced shifts in productivity or runoff of terrigenous material from glacial or glacifluvial meltwater sourced from distant ice sheet margins, although further geochemical and sedimentological analysis would be required to assess this.

RSS3-I depocenters in the western Ross Sea are located in the outer part of the Joides and Central basins (Fig. 9). The lithological pattern observed at DSDP Site 273 in this interval is also consistent with reduced ice sheet extent, and relates to steady delivery of hemipelagic muds, potentially related to terrigenous outwash from the Transantarctic Mountains, with intermittent periods of higher biological productivity (diatom-rich muds), as well as higher sand content, with the latter suggesting either periods of increased proximity of grounded ice or changes in relative sea level (Hayes et al., 1975; Balshaw, 1981).

RSU4a to D-a (RSS4-II): Aggradational Deposition and Episodic Ice Advance

The sharpest porosity change in Package B corresponds to discontinuity RSU4a in the Pennell Basin (Fig. 5). The underlying sediment is more lithified, compared to the overlying record as interpreted from the velocities from the tomography model (Supplemental Fig. S3). RSU4a represents an apparent truncation in the seismic record in the Pennell Basin, particularly along the Pennell Bank margin (Fig. 3B). However, tracing this discontinuity is complicated by lateral seismic facies changes similar to those in the diatom-rich sediments forming RSS3-Ia where they underwent opal A/CT transformation. As noted above, diatom deposition is likely to be highly focused into the depocenters of each basin, thereby forming isolated chert layers across the Ross Sea basins. Directly overlying the chert layers in IODP Site U1521 are carbonate cemented diatom-bearing diamictites, interbedded with thin diatom-rich mudstones (Fig. 4B).

Besides the local truncation signature of RSU4a, the three studied sites contain distinct seismic patterns within RSS4-II. The AND-2A Site record suggests a predominately terrestrial-based ice sheet fluctuated in extent during glacial-interglacial cycles between ca. 17.1 and ca. 16.2 Ma (Levy et al., 2016), just following the interpreted RSU4a event. Although there is no clear evidence in the seismic record of a shelf-wide marine-based ice sheet advance, progradation of glacimarine deposits is evident at both IODP Site U1521 and DSDP Site 273, with diamicts and muds with high sand content being deposited above RSU4a (Fig. 4). After ca. 17 Ma, the chaotic facies of the RSS4-IIb, and the ice-distal glacimarine sediments at DSDP Site 273 (Balshaw, 1981; Hambrey and Barrett, 1993), suggest EAIS advances were relatively limited in extent, potentially restricted to the coastal regions of the Transantarctic Mountains. Glacimarine seismically-imaged semi-transparent diamictites in RSS4-IIb are aggradational in nature, suggesting that although marine-terminating glacial systems were present in the region, either sediment supply was greatly

reduced relative to the progradational deposits of RSS3-II, or this was a shorter duration advance. The stratified seismic facies identified in RSS4-IIa in the Pennell Basin are consistent with a transition toward more ice-distal glacimarine conditions (Figs. 3A and 3B), coinciding with an ~0.8‰ $\delta_{18}O$ decrease in global benthic stacks (Levy et al., 2019). Equally, sparse morainal banks are identified in the eastern Ross Sea within RSS4-II, which could be related to marine-terminating glaciers sourced from an inland ice sheet (Figs. 8A and 11). This unit represents a short-lived ice advance at ca. 16.9 Ma over the inner continental shelf of the Ross Sea, followed by a retreat of marine-terminating ice through 16.7 Ma.

D-a to RSU4 (RSS4-I): Open Marine Deposition and Widespread Ice Retreat

RSS4-I is identified exclusively in Pennell Basin, Pennell Bank, and Joides Basin, showing very high porosity values (up to 80%) (Figs. 3B and 5) and particularly low velocities (1400–2000 m/s) (Figs. 4 and 5). The high porosity is likely related to the high diatom content identified in this unit (Hayes et al., 1975; McKay et al., 2019). In addition, the FMS images show highly conductive sediments forming RSS4-I at IODP Site U1521. In the Joides Basin, mudstone characterized by intervals of high diatom content (~30–35%) occurs just above the D-a unconformity (ca. 16.7 Ma), whereas diatoms are less abundant (<10%) at depths above this (Hayes et al., 1975). In the Glomar Challenger Basin at DSDP Site 272, most of this interval is missing due to the prior shift in the basin depocenter (Fig. 9). However, a thin interval (~12 m) between ca. 15.8 and 15.3 Ma is present and has higher diatom abundances (diatomites) than intervals above (diamictite) and below (diatom-bearing to diatom-rich mudstones) (Hayes et al., 1975). High conductivity, together with low values of density and natural gamma radiation (Fig. 5), reveal a high productivity period during the formation of RSS4-I, where biogenic sedimentation was focused into the Pennell Basin and the eastern margin of the Joides Basin during the time period between D-a and RSU4 formation, currently dated as 16.7–14.6 Ma (Table 2). The aggradational pattern and overall stratified, low amplitude facies of RSS4-I points to prevalent inland ice retreat, and pelagic and hemipelagic suspension settling in the basin depocenters. The current age control indicates that RSS4-I was deposited during the global warmth of the MCO. Ice sheet models, inland outcrops, and coastal sediment cores suggest significant retreat of the EAIS into the continental interior during the interglacials of the MCO (Gasson et al., 2016; Levy et al., 2016). According to the nature of RSS4-I from seismic profiles across the Pennell and Joides basins, and using the basic assumption of a linear sedimentation rate for this unit, ~110 m of stratigraphically conformable sediments overlies this unit to the northwest of IODP Site U1521 on the Pennell Bank (Fig. 3B). Therefore, it is likely that only the oldest preserved strata of RSS4-I were recovered at IODP Site U1521 (Table 2; Fig. 4). The RSU4 erosional surface marks the end of the MCO warm interval and has potentially removed up to ~1.2 m.y. of the uppermost interval of the RSS4-I from IODP Site U1521 (McKay et al., 2019).

The Middle Miocene Climate Transition and Subsequent Marine-Based Ice Sheet Advances (<14.6 Ma)

At the top of Package B, RSU4 shows as a well-defined surface that truncates underlying strata and shows tunnel valley features (Figs. 3B, 4B, and 11). Earlier seismic and drill core records have indicated major advances of a large ice sheet over the continental shelf of the Ross Sea during the MMCT (De Santis et al., 1995; Levy et al., 2016).

The sediment distribution of the overlying Package A is thickest along the modern shelf edge of the eastern Ross Sea (Fig. 7). However, the thin sedimentary record (<0.05 s TWTT) on the inner to middle continental shelf highlights the prevalence of non-deposition and erosional processes in the central Ross Sea from the mid-Miocene onwards (Fig. 11). Highly concentrated locations of sedimentation through the build-up of the Ross and Pennell banks (Fig. 7) are inferred to be the consequence of localized deposition at the confluence of adjoining ice streams of a marine-based ice sheet extended to the continental shelf edge (Bart and De Santis, 2012). Erosional and depositional processes related to the marine-based ice sheet emanating from both the WAIS and EAIS intensified, with regular shelf wide advances during this period (Anderson and Bartek, 1992; De Santis et al., 1999; Bart, 2003; Naish et al., 2009; Levy et al., 2019). In similar lithologies, lower porosity values in the Pennell Basin (~30%) with respect to the neighboring basins (60–80%) could point to higher compaction degree (Fig. 5; Supplemental Material). The facies in the lithostratigraphic units I and II of IODP Site U1521 indicate highly truncated cycles of subglacial, glaciomarine, and open marine sedimentation (McKay et al., 2019). Thus, repetitive advances of the marine-based ice sheet over U1521 occurred since RSU4 formation. At the DSDP Site 273 in the Joides Basin, Plio-Pleistocene sediments in the upper 26 m comprise diamictites that lay directly over the highly erosional RSU4 surface, suggestive of a similar depositional process as at IODP Site U1521 and numerous ice sheet overriding events since RSU4 time (Hayes et al., 1975; Balshaw, 1981; Bart, 2003). Diatom-bearing diamictites dominate DSDP Site 272 in the Glomar Challenger Basin (Balshaw, 1981), where the package is much thicker (0.1–0.8 s TWTT) than in the other basins but contains a prograding geometry interpreted as an ice-proximal feature (Figs. 6 and 7) (De Santis et al., 1997). Package A in Glomar Challenger Basin is inferred to represent significant volumes of glacimarine deposition at the margin of the marine-terminating ice sheets that reached the paleo-continental shelf edge in that region (McKay et al., 2019). The chaotic and tilted reflections identified in the upper seismic sequence of Package A and the widespread erosional surfaces (Figs. 3B and 6) record the multiple marine-based ice sheet grounding episodes that have previously been interpreted during late Miocene to Pleistocene times in the Ross Sea (e.g., Alonso et al., 1992; Anderson and Bartek, 1992; Bart, 2003; Chow and Bart, 2003; Naish et al., 2009; McKay et al., 2009; Levy et al., 2016).

CONCLUSIONS

Core-log-seismic correlation analyses on the Ross Sea continental shelf reveal a dynamic glacial history during the early and middle Miocene. Changes in sedimentary depocenters, seismic facies, and physical properties reveal open marine, ice-distal to ice-proximal glacimarine and subglacial conditions occurred in a heterogeneous manner across the continental shelf of the Ross Sea at various times through the past ~23 m.y.

Isolated ice-proximal and regional ice-distal conditions are interpreted to occur during the early Miocene prior to the formation of RSU5, i.e., before ca. 18 Ma. An aggradational stratigraphic pattern below RSU5 points to glaciomarine to open marine conditions correlating with an interval of long-term regional sea level rise driven by glacial isostatic adjustment of the pre-established morphology in response to grounded ice loads that were limited to the bathymetric highs along the western Ross Sea.

Episodic growth of marine-terminating glaciers and ice sheets occurred during periods of prevailing colder climatic conditions of the latest early and middle Miocene (ca. 18–14.6 Ma). Widespread prograding wedges suggest glacimarine to subglacial environmental conditions in the Ross Sea between ca. 18 and 17.4 Ma, when localized grounded ice could have expanded and flowed from and beyond local bathymetric highs. Such ice caps could have nucleated around remaining subaerial areas in the Pennell

Bank prior to final subsidence and erosion below sea level in the middle Miocene. Alternately, the grounding of ice shelves onto bathymetric highs could have resulted in the subsequent formation of an ice rise. These ice caps, as well as the main ice sheets, fed the marine-terminating glaciers, which delivered sediment to their grounding zones forming morainal bank complexes preserved in the southern part of the Glomar Challenger Basin and the Ross Bank.

Periods of ice edge retreat before ca. 17 Ma correlate with a period of eustatic sea level rise and southward migration of the identified morainal bank complexes. The increased areal extent of open marine conditions across the Ross Sea continental shelf led to local depocenters of diatom-rich sedimentation. Subsequent burial of these biosiliceous muds resulted in the formation of opal diagenetic fronts which created chert layers in restricted areas. Episodic ice expansion over the inner Ross Sea continental shelf and local highs between ca. 17 and 16.7 Ma is inferred from the chaotic seismic facies and the sediments retrieved from Joides Basin, together with the identification of sparse morainal bank complexes associated with marine-terminating glaciers in the eastern Ross Sea. Ice-distal environmental conditions prevailed on the continental shelf of the Ross Sea after ca. 16.7 Ma during the warmest period of the MCO. The aggradational pattern of the biogenic sediments retrieved from the sedimentary basins reveals inland ice retreat, and pelagic and hemipelagic suspension settling forming the basin depocenters.

RSU4 formed during the MMCT through ice sheet advances that eroded over ~110 m of the sedimentary record of the Pennell Basin. The regional erosive signature of RSU4 suggests the onset of cycles of marine-based ice sheet advance and retreat extending toward the outer margin of the continental shelf edge occurred after ca. 14.6 Ma. Since the mid-Miocene, inclined chaotic seismic facies and widespread erosional surfaces identified in the sedimentary record testify to the multiple marine-based ice sheet grounding episodes in the Ross Sea. Provenance tracing using geochemical analysis, paleo-temperatures, and paleodepth bathymetric reconstructions will help to further assess how the sediment delivery pathways may relate to the presence or absence of local ice caps, or large scale EAIS/WAIS advance during these time periods, and will be the focus of future work pertaining to IODP Expedition 374.

ACKNOWLEDGMENTS

This project has received funding from the European Union's Horizon 2020 research and innovation program under the Marie Sklodowska-Curie grant agreement number 792773 for the West Antarctic Margin Signatures of Ice Sheet Evolution Project. The work was fully developed during two consecutive research stays of the first author at the National Institute of Oceanography and Applied Geophysics (Trieste, Italy) and the Antarctic Research Centre at Victoria University of Wellington (Wellington, New Zealand). This project used data provided by the International Ocean Discovery Program (IODP). It is in the frame of National Antarctic Research Program PNRA16_00016 project and the British Antarctic Survey (BAS) Polar Science for Planet Earth Program. RMM was funded by the Royal Society of New Zealand Te Apārangi Marsden Fund (grant 18-VUW-089). RMM, RHL, and TRN acknowledge the funding support providing by the New Zealand Ministry of Business, Innovation and Employment through the Antarctic Science Platform (ANTA1801). JSL acknowledges the support from European Consortium for Ocean Research Drilling and the Research Council of Norway allowing for his participation on Expedition 374 and the post-cruise work. Most of the multichannel seismic profiles used in this work are available at the Antarctic Seismic Data Library System (https://sdls.ogs.trieste.it) under the auspices of the Scientific Committee on Antarctic Research (SCAR) policy. In addition, the PD90 single channel seismic data available thought the collaboration with J.B. Anderson and L. Bartek have been crucial for this work. We acknowledge S. Henrys participation in the seismic data compilation. We are also grateful to N. Wardell of the National Institute of Oceanography and Applied Geophysics (OGS), Trieste, Italy, for his help with seismic technical issues. The seismic processing has been carried out with academic licenses from Emerson Paradigm for Echos software. The IHS-Kingdom project was supported through academic licenses released to OGS and BAS. Our heartfelt acknowledgment to the captain, crew, and technicians of the *JOIDES Resolution* who made IODP Expedition 374 possible. This research is a contribution to the SCAR program Past Antarctic Ice Sheet Dynamics. In addition, this work further contributes to the SCAR program Instabilities and Thresholds in Antarctica: The Antarctic contribution to global sea-level. We acknowledge the review of Karsten Gohl and an anonymous reviewer which greatly improved the initial version of this work.

REFERENCES CITED

Alonso, B., Anderson, J.B., Díaz, J.I., and Bartek, L.R., 1992, Pliocene–Pleistocene seismic stratigraphy of the Ross Sea: Evidence for multiple ice sheet grounding episodes, *in* Elliot, D.H., ed., Contribution to Antarctic Research III: Washington, D.C., American Geophysical Union, Antarctic Research Series, v. 57, p. 93–103, https://doi.org/10.1029/AR057p0093.

Anderson, J.B., and Bartek, L.R., 1992, Cenozoic glacial history of the Ross Sea revealed by intermediate resolution seismic reflection data combined with drill site information: The Antarctic Paleoenvironment: A Perspective on Global Change: Part One, v. 56, p. 231–263.

Anderson, J.B., Conway, H., Bart, P.J., Witus, A.E., Greenwood, S.L., McKay, R.M., Hall, B.L., Ackert, R.P., Licht, K., Jakobsson, M., and Stone, J.O., 2014, Ross Sea paleo-ice sheet drainage and deglacial history during and since the LGM: Quaternary Science Reviews, v. 100, p. 31–54, https://doi.org/10.1016/j.quascirev.2013.08.020.

Anderson, J. B., Simkins, L. M., Bart, P. J., De Santis, L., Halberstadt, A. R. W., Olivo, E., and Greenwood, S. L., 2019, Seismic and geomorphic records of Antarctic Ice Sheet evolution in the Ross Sea and controlling factors in its behaviour, v. 475, no. 1, p. 223–240.

Arndt, J.E., Werner, S.H., Jakobsson, M., Nitsche, F.O., Buys, G., Goleby, B., Robesco, M., Bohoyo, F., Hong, J., Black, J., Greku, R., Udintsev, G., Barrios, F., Reynoso-Perlata, W., Taisei, M., and Wigley, R., 2013, The International Bathymetric Chart of the Southern Ocean (IBCSO) Version 1.0: A new bathymetric compilation covering circum-Antarctic waters: Geophysical Research Letters, v. 40, p. 3111–3117, https://doi.org/10.1002/grl.50413.

Balshaw, K.M., 1981, Antarctic glacial chronology reflected in the Oligocene through Pliocene sedimentary section in the Ross Sea [Ph.D. thesis]: Houston, Texas, Rice University, 182 p.

Balter-Kennedy, A., Bromley, G., Balco, G., Thomas, H., and Jackson, M.S., 2020, A 14.5-million-year record of East Antarctic Ice Sheet fluctuations from the central Transantarctic Mountains, constrained with cosmogenic ^{3}He, ^{10}Be, ^{21}Ne, and ^{26}Al: The Cryosphere, v. 14, no. 8, p. 2647–2672, https://doi.org/10.5194/tc-14-2647-2020.

Barrett, P.J., 2007, Cenozoic climate and sea level history from glacimarine strata off the Victoria Land Coast, Cape Roberts Project, Antarctica, *in* Hambrey, M.J., Christoffersen, P., Glasser, N.F., and Hubbart, B., eds., Glacial Sedimentary Processes and Products: International Association of Sedimentologists Special Publication, p. 259–287, https://doi.org/10.1002/9781444304435.ch15.

Barrett, P.J., 1989, Antarctic Cenozoic history from the CIROS-1 drillhole, McMurdo Sound: DSIR Bulletin, v. 245, Wellington, New Zealand, Science Information Publishing Centre, 254 p.

Bart, P.J., 2003, Were West Antarctic Ice Sheet grounding events in the Ross Sea a consequence of East Antarctic Ice Sheet expansion during the middle Miocene?: Earth and Planetary Science Letters, v. 216, no. 1–2, p. 93–107, https://doi.org/10.1016/S0012-821X(03)00509-0.

Bart, P.J., and Anderson, J.B., 2000, Relative temporal stability of the Antarctic ice sheets during the late Neogene based on the minimum frequency of outer shelf grounding events: Earth and Planetary Science Letters, v. 182, no. 3–4, p. 259–272, https://doi.org/10.1016/S0012-821X(00)00257-0.

Bart, P., and De Santis, L., 2012, Glacial intensification during the Neogene: A review of seismic stratigraphic evidence from the Ross Sea, Antarctica, continental shelf: Oceanography (Washington, D.C.), v. 25, no. 3, p. 166–183, https://doi.org/10.5670/oceanog.2012.92.

Bart, P.J., Anderson, J.B., Trincardi, F., and Shipp, S.S., 2000, Seismic data from the Northern basin, Ross Sea, record extreme expansions of the East Antarctic Ice Sheet during the late Neogene: Marine Geology, v. 166, no. 1–4, p. 31–50, https://doi.org/10.1016/S0025-3227(00)00006-2.

Bartek, L.R., Vail, P.R., Anderson, J.B., Emmet, P.A., and Wu, S., 1991, Effect of Cenozoic ice sheet fluctuations in Antarctica on the stratigraphic signature of the Neogene: Journal of Geophysical Research. Solid Earth, v. 96, p. 6753–6778, https://doi.org/10.1029/90JB02528.

Bohrmann, G., Spieß, V., Hinze, H., and Kuhn, G., 1992, Reflector "Pc" a prominent feature in the Maud Rise sediment sequence (eastern Weddell Sea): Occurrence, regional distribution and implications to silica diagenesis: Marine Geology, v. 106, no. 1, p. 69–87, https://doi.org/10.1016/0025-3227(92)90055-M.

Brancolini, G., Busetti, M., Marchetti, A., De Santis, L., Zanolla, C., Cooper, A.K., Cochrane, G.R., Zayatz, I., Belyaev, V., Knyazev, M., Vinnikovskaya, O., Davey, F.J., and Hinz, K., 1995, Descriptive text for the Seismic Stratigraphic Atlas of the Ross Sea, *in* Cooper, A., Barker, P.F., and Brancolini, G., eds., Geology and Seismic Stratigraphy of the Antarctic Margin: Washington, D.C., American Geophysical Union, Antarctic Research Series, v. 68, p. A271–A268.

Brook, E.J., Brown, E.T., Kurz, M.D., Ackert, R.P., Jr., Raisbeck, G.M., and Yiou, F., 1995, Constraints on age, erosion, and uplift of Neogene glacial deposits in the Transantarctic Mountains determined from in situ cosmogenic 10Be and 26Al: Geology, v. 23, no. 12, p. 1063–1066, https://doi.org/10.1130/0091-7613(1995)023<1063:COAEAU>2.3.CO;2.

Busetti, M., De Santis, L., Kavun, M., and Zayatz, I., 1993, Seismic sequences of the Ross Sea continental margin

(Antarctica): Bollettino di Geofisica Teorica ed Applicata, v. 35, no. 137-138, p. 133–152.

Cande, S.C., Stock, J.M., Müller, R.D., and Ishihara, T., 2000, Cenozoic motion between East and West Antarctica: Nature, v. 404, p. 145–150, https://doi.org/10.1038/35004501.

Chow, J.M., and Bart, P.J., 2003, West Antarctic Ice Sheet grounding events on the Ross Sea outer continental shelf during the middle Miocene: Palaeogeography, Palaeoclimatology, Palaeoecology, v. 198, no. 1, p. 169–186, https://doi.org/10.1016/S0031-0182(03)00400-0.

Colleoni, F., De Santis, L., Siddoway, C.S., Bergamasco, A., Golledge, N.R., Lohmann, G., Passchier, S., and Siegert, M.J., 2018, Spatio-temporal variability of processes across Antarctic ice-bed-ocean interfaces: Nature Communications, v. 9, no. 2289, https://doi.org/10.1038/s41467-018-04583-0.

Cook, C.P., van de Flierdt, T., Williams, T., Hemming, S.R., Iwai, M., Kobayashi, M., Jimenez-Espejo, F.J., Escutia, C., González, J.J., Khim, B.-K., McKay, R.M., Passchier, S., Bohaty, S.M., Riesselman, C.R., Tauxe, L., Sugisaki, S., Galindo, A.L., Patterson, M.O., Sangiorgi, F., Pierce, E.L., Brinkhuis, H., Klaus, A., Fehr, A., Bendle, J.A.P., Bijl, P.K., Carr, S.A., Dunbar, R.B., Flores, J.A., Hayden, T.G., Katsuki, K., Kong, G.S., Nakai, M., Olney, M.P., Pekar, S.F., Pross, J., Röhl, U., Sakai, T., Shrivastava, P.K., Stickley, C.E., Tuo, S., Welsh, K., and Yamane, M., 2013, Dynamic behaviour of the East Antarctic ice sheet during Pliocene warmth: Nature Geoscience, v. 6, no. 9, p. 765–769, https://doi.org/10.1038/ngeo1889.

Cooper, A.K., and Davey, F.J., 1987, The Antarctic continental margin: Geology and geophysics of the western Ross Sea: Houston, Texas, USA, Circum-Pacific Council for Energy and Mineral Resources, Earth Science Series, v. 5B.

Cooper, A.K., Barrett, P.J., Hinz, K., Traube, V., Letichenkov, G., and Stagg, H.M.J., 1991, Cenozoic prograding sequences of the Antarctic continental margin: A record of glacio-eustatic and tectonic events: Marine Geology, v. 102, no. 1–4, p. 175–213, https://doi.org/10.1016/0025-3227(91)90008-R.

Cooper, A.K., Barker, P.F., and Brancolin, G., 1995, Geology and Seismic Stratigraphy of the Antarctic Margin: Washington, D.C., USA, American Geophysical Union, Antarctic Research Series, v. 68, 303 p.

Cramer, B.S., Miller, K.G., Barrett, P.J., and Wright, J.D., 2011, Late Cretaceous–Neogene trends in deep ocean temperature and continental ice volume: Reconciling records of benthic foraminiferal geochemistry ($\delta^{18}O$ and Mg/Ca) with sea level history: Journal of Geophysical Research. Oceans, v. 116, no. C12, https://doi.org/10.1029/2011JC007255.

Davey, F.J., and Brancolini, G., 1995, The late Mesozoic and Cenozoic structural setting of the Ross Sea region, *in* Cooper, A.J., Barker, P.F., and Brancolini, G., eds., Geology and Seismic Stratigraphy of the Antarctic Margin: Washington, D.C., USA, American Geophysical Union, Antarctic Research Series, v. 68, p. 167–182.

Davies, R.J., and Cartwright, J., 2002, A fossilized Opal A to Opal C/T transformation on the northeast Atlantic margin: Support for a significantly elevated palaeogeothermal gradient during the Neogene?: Basin Research, v. 14, no. 4, p. 467–486, https://doi.org/10.1046/j.1365-2117.2002.00184.x.

De Santis, L., Anderson, J.B., Brancolini, G., and Zayatz, I., 1995, Seismic record of late Oligocene through Miocene glaciation on the central and eastern continental shelf of the Ross Sea: Geology and Seismic Stratigraphy of the Antarctic Margin, v. 68, p. 235–260.

De Santis, L., Anderson, J.B., Brancolini, G., and Zayatz, I., 1997, Glacio-Marine Deposits on the Continental Shelf of Ross Sea, Antarctica, *in* Davies, T.A., Bell, T., Cooper, A.K., Josenhans, H., Polyak, L., Solheim, A., Stoker, M.S., and Stravers, J.A., eds., Glaciated Continental Margins: An Atlas of Acoustic Images: Dordrecht, The Netherlands, Springer, p. 110–113.

De Santis, L., Prato, S., Brancolini, G., Lovo, M., and Torelli, L., 1999, The Eastern Ross Sea continental shelf during the Cenozoic: Implications for the West Antarctic ice sheet development: Global and Planetary Change, v. 23, no. 1, p. 173–196, https://doi.org/10.1016/S0921-8181(99)00056-9.

Dell, R.K., and Fleming, C.A., 1975, Oligocene-Miocene bivalve Mollusca and other macrofossils from sites 270 and 272 (Ross Sea), DSDP, Leg 28, *in* Hayes, D.E., Frakes, L.A., Barrett, P.J., Burns, D.A., Chen, P.-H., Ford, A.B., Kaneps, A.G., Kemp, E.M., McCollum, D.W., Piper, D.J.W., Wall, R.E., and Webb, P.N., eds., Initial Reports of the Deep Sea Drilling Project: College Station, Texas, Deep Sea Drilling Project Reports and Publications v. 28, p. 693–703.

Denton, G.H., and Hughes, T.J., 2002, Reconstructing the Antarctic Ice Sheet at the Last Glacial Maximum: Quaternary Science Reviews, v. 21, no. 1, p. 193–202, https://doi.org/10.1016/S0277-3791(01)00090-7.

Dowdeswell, J.A., Hogan, K.A., Arnold, N.S., Mugford, R.I., Wells, M., Hirst, J.P.P., Decalf, C., and Eyles, N., 2015, Sediment-rich meltwater plumes and ice-proximal fans at the margins of modern and ancient tidewater glaciers: Observations and modelling: Sedimentology, v. 62, no. 6, p. 1665–1692, https://doi.org/10.1111/sed.12198.

Dunbar, R.B., Anderson, J.B., Domack, E.W., and Jacobs, S.S., 1985, Oceanographic Influences on sedimentation along the Antarctic Continental Shelf, *in* Jacobs, S.S., ed., Oceanology of the Antarctic Continental Shelf: Washington, D.C., USA, American Geophysical Union, Antarctic Research Series, v. 43, p. 291–312, https://doi.org/10.1029/AR043p0291.

Escutia, C., Brinkhuis, H., and Klaus, A., 2011, IODP Expedition 318: From greenhouse to icehouse at the Wilkes Land Antarctic margin: Scientific Drilling, v. 12, p. 15–23, https://doi.org/10.2204/iodp.sd.12.02.2011.

Feakins, S.J., Warny, S., and Lee, J.-E., 2012, Hydrologic cycling over Antarctica during the middle Miocene warming: Nature Geoscience, v. 5, no. 8, p. 557–560, https://doi.org/10.1038/ngeo1498.

Fielding, C.R., 2018, Stratigraphic architecture of the Cenozoic succession in the McMurdo Sound region, Antarctica: An archive of polar palaeoenvironmental change in a failed rift setting: Sedimentology, v. 65, no. 1, p. 1–61, https://doi.org/10.1111/sed.12413.

Fielding, C.R., Browne, G.H., Field, B., Florindo, F., Harwood, D.M., Krissek, L.A., Levy, R.H., Panter, K.S., Passchier, S., and Pekar, S.F., 2011, Sequence stratigraphy of the ANDRILL AND-2A drillcore, Antarctica: A long-term, ice-proximal record of Early to Mid-Miocene climate, sea-level and glacial dynamism: Palaeogeography, Palaeoclimatology, Palaeoecology, v. 305, no. 1–4, p. 337–351, https://doi.org/10.1016/j.palaeo.2011.03.026.

Fitzgerald, P.G., 1992, The Transantarctic Mountains of southern Victoria Land: The application of apatite fission track analysis to a rift shoulder uplift: Tectonics, v. 11, no. 3, p. 634–662, https://doi.org/10.1029/91TC02495.

Flower, B.P., and Kennett, J.P., 1994, The middle Miocene climatic transition: East Antarctic ice sheet development, deep ocean circulation and global carbon cycling: Palaeogeography, Palaeoclimatology, Palaeoecology, v. 108, no. 3–4, p. 537–555, https://doi.org/10.1016/0031-0182(94)90251-8.

Gasson, E., DeConto, R.M., Pollard, D., and Levy, R.H., 2016, Dynamic Antarctic ice sheet during the early to mid-Miocene: Proceedings of the National Academy of Sciences of the United States of America, v. 113, no. 13, p. 3459–3464, https://doi.org/10.1073/pnas.1516130113.

Goldner, A., Herold, N., and Huber, M., 2014, The challenge of simulating the warmth of the mid-Miocene climatic optimum in CESM1: Climate of the Past, v. 10, no. 2, p. 523–536, https://doi.org/10.5194/cp-10-523-2014.

Golledge, N.R., Levy, R.H., McKay, R.M., Fogwill, C.J., White, D.A., Graham, A.G.C., Smith, J.A., Hillenbrand, C.-D., Licht, K.J., Denton, G.H., Ackert, R.P., Jr., Maas, S.M., and Hall, B.L., 2013, Glaciology and geological signature of the Last Glacial Maximum Antarctic ice sheet: Quaternary Science Reviews, v. 78, p. 225–247, https://doi.org/10.1016/j.quascirev.2013.08.011.

Granot, R., and Dyment, J., 2018, Late Cenozoic unification of East and West Antarctica: Nature Communications, v. 9, no. 3189, https://doi.org/10.1038/s41467-018-05270-w.

Gulick, S.P.S., Shevenell, A.E., Montelli, A., Fernandez, R., Smith, C., Warny, S., Bohaty, S.M., Sjunneskog, C., Leventer, A., Frederick, B., and Blankenship, D.D., 2017, Initiation and long-term instability of the East Antarctic Ice Sheet: Nature, v. 552, no. 7684, p. 225–229, https://doi.org/10.1038/nature25026.

Hambrey, M.J., and Barrett, P.J., 1993, Cenozoic sedimentary and climatic record, Ross Sea region, Antarctica, *in* Kennett, J.P., and Warnke, D.A., eds., The Antarctic Paleoenvironment: A Perspective on Global Change: Part Two: Washington, D.C., American Geophysical Union, Antarctic Research Series, v. 60, p. 91–124.

Haq, B.U., Hardenbol, J., and Vail, P.R., 1987, Chronology of fluctuating sea levels since the Triassic: Science, v. 235, p. 1156–1167, https://doi.org/10.1126/science.235.4793.1156.

Hayes, D.E., and Frakes, L.A., 2004a, Wet bulk density (GRAPE) of Hole 28-272: PANGAEA, https://doi.pangaea.de/10.1594/PANGAEA.224665.

Hayes, D.E., and Frakes, L.A., 2004b, Wet bulk density (GRAPE) of Hole 28-273, PANGAEA, https://doi.org/10.1594/PANGAEA.224666.

Hayes, D.E., Frakes, L.A., Barrett, P.J., Burns, D.A., Chen, P.-H., Ford, A.B., Kaneps, A.G., Kemp, E.M., McCollum, D.W., Piper, D.J.W., Wall, R.E., and Webb, P.N., 1975, Initial Reports of the Deep Sea Drilling Project: College Station, Texas, Deep Sea Drilling Project Reports and Publications, v. 28, https://doi.org/10.2973/dsdp.proc.28.1975.

Hein, J.R., Scholl, D.W., Barron, J.A., Jones, M.G., and Miller, J., 1978, Diagenesis of late Cenozoic diatomaceous deposits and formation of the bottom simulating reflector in the southern Bering Sea: Sedimentology, v. 25, no. 2, p. 155–181, https://doi.org/10.1111/j.1365-3091.1978.tb00307.x.

Hinz, K., and Block, M., 1984, Results of geophysical investigations in the Weddell Sea and in the Ross Sea, Antarctica, *in* Proceedings of the 11th World Petroleum Congress: Chichester, London, UK, John Wiley & Sons, Geology Exploration Reserves, v. 2, p. 79–91.

Hochmuth, K., and Gohl, K., 2019, Seaward growth of Antarctic continental shelves since establishment of a continent-wide ice sheet: Patterns and mechanisms: Palaeogeography, Palaeoclimatology, Palaeoecology, v. 520, p. 44–54, https://doi.org/10.1016/j.palaeo.2019.01.025.

Holbourn, A., Kuhnt, W., Clemens, S., Prell, W., and Andersen, N., 2013, Middle to late Miocene stepwise climate cooling: Evidence from a high-resolution deep water isotope curve spanning 8 million years: Paleoceanography, v. 28, no. 4, p. 688–699, https://doi.org/10.1002/2013PA002538.

Holbourn, A., Kuhnt, W., Lyle, M., Schneider, L., Romero, O., and Andersen, N., 2014, Middle Miocene climate cooling linked to intensification of eastern equatorial Pacific upwelling: Geology, v. 42, no. 1, p. 19–22, https://doi.org/10.1130/G34890.1.

Isaacs, N.S., 1981, Physical methods. Part (iii) high-pressure chemistry: Annual Reports on the Progress of Organic Chemistry Section B, v. 78, p. 29–38, https://doi.org/10.1039/oc9817800029.

John, C.M., Karner, G.D., Browning, E., Leckie, R.M., Mateo, Z., Carson, B., and Lowery, C., 2011, Timing and magnitude of Miocene eustasy derived from the mixed siliciclastic-carbonate stratigraphic record of the northeastern Australian margin: Earth and Planetary Science Letters, v. 304, no. 3–4, p. 455–467, https://doi.org/10.1016/j.epsl.2011.02.013.

Karner, G.D., Studinger, M., and Bell, R.E., 2005, Gravity anomalies of sedimentary basins and their mechanical implications: Application to the Ross Sea basins, West Antarctica: Earth and Planetary Science Letters, v. 235, no. 3, p. 577–596, https://doi.org/10.1016/j.epsl.2005.04.016.

Kehew, A.E., Piotrowski, J.A., and Jørgensen, F., 2012, Tunnel valleys: Concepts and controversies: A review: Earth-Science Reviews, v. 113, no. 1, p. 33–58, https://doi.org/10.1016/j.earscirev.2012.02.002.

Kender, S., Yu, J., and Peck, V.L., 2014, Deep ocean carbonate ion increase during mid Miocene CO_2 decline: Scientific Reports, v. 4, no. 4187, https://doi.org/10.1038/srep04187.

Kennett, J.P., 1977, Cenozoic evolution of Antarctic glaciation, the Circum-Antarctic ocean, and their impact on global paleoceanography: Journal of Geophysical Research. Oceans and Atmospheres, v. 82, p. 3843–3860, https://doi.org/10.1029/JC082i027p03843.

Kim, S., De Santis, L., Hong, J.K., Cottlerle, D., Petronio, L., Colizza, E., Kim, Y.-G., Kang, S.-G., Kim, H.J., Kim, S., Wardell, N., Geletti, R., Bergamasco, A., McKay, R., Jin, Y.K., and Kang, S.-H., 2018, Seismic stratigraphy of the Central Basin in northwestern Ross Sea slope and rise, Antarctica: Clues to the late Cenozoic ice-sheet dynamics and bottom-current activity: Marine Geology, v. 395, p. 363–379, https://doi.org/10.1016/j.margeo.2017.10.013.

Kominz, M.A., Browning, J.V., Miller, K.G., Sugarman, P.J., Mizintseva, S., and Scotese, C.R., 2008, Late Cretaceous to Miocene sea-level estimates from the New Jersey and Delaware coastal plain coreholes: An error analysis: Basin Research, v. 20, no. 2, p. 211–226, https://doi.org/10.1111/j.1365-2117.2008.00354.x.

Kominz, M.A., Miller, K.G., Browning, J.V., Katz, M.E., and Mountain, G.S., 2016, Miocene relative sea level on the New Jersey shallow continental shelf and coastal plain derived from one-dimensional backstripping: A case for both eustasy and epeirogeny: Geosphere, v. 12, no. 5, p. 1437–1456, https://doi.org/10.1130/GES01241.1.

Larter, R.D., Graham, A.G.C., Hillenbrand, C.-D., Smith, J.A., and Gales, J.A., 2012, Late Quaternary grounded ice extent in the Filchner Trough, Weddell Sea, Antarctica: New marine geophysical evidence: Quaternary Science Reviews, v. 53, p. 111–122, https://doi.org/10.1016/j.quascirev.2012.08.006.

Lavoie, C., Domack, E.W., Pettit, E.C., Scambos, T.A., Larter, R.D., Schenke, H.W., Yoo, K.C., Gutt, J., Wellner, J., Canals, M., Anderson, J.B., and Amblas, D., 2015, Configuration of the Northern Antarctic Peninsula Ice Sheet at LGM based on a new synthesis of seabed imagery: The Cryosphere, v. 9, no. 2, p. 613–629, https://doi.org/10.5194/tc-9-613-2015.

Leckie, R.M., and Webb, P.N., 1983, Late Oligocene-early Miocene glacial record of the Ross Sea, Antarctica: Evidence from DSDP Site 270: Geology, v. 11, no. 10, p. 578–582, https://doi.org/10.1130/0091-7613(1983)11<578:LOMGRO>2.0.CO;2.

Levy, R., Harwood, D., Florindo, F., Sangiorgi, F., Tripati, R., Von Eynatten, H., Gasson, E., Kuhn, G., Tripati, A., DeConto, R., Fielding, C., Field, B., Golledge, N., McKay, R., Naish, T., Olney, M., Pollard, D., Schouten, S., Talarico, F., Warny, S., Willmott, V., Acton, G., Panter, K., Paulsen, T., and Taviani, M., 2016, Antarctic ice sheet sensitivity to atmospheric CO_2 variations in the early to mid-Miocene: Proceedings of the National Academy of Sciences of the United States of America, v. 113, no. 13, p. 3453–3458, https://doi.org/10.1073/pnas.1516030113.

Levy, R.H., Meyers, S.R., Naish, T.R., Golledge, N.R., McKay, R.M., Crampton, J.S., DeConto, R.M., De Santis, L., Florindo, F., Gasson, E.G.W., Harwood, D.M., Luyendyk, B.P., Powell, R.D., Clowes, C., and Kulhanek, D.K., 2019, Antarctic ice-sheet sensitivity to obliquity forcing enhanced through ocean connections: Nature Geoscience, v. 12, no. 2, p. 132–137, https://doi.org/10.1038/s41561-018-0284-4.

Lewis, A.R., Marchant, D.R., Kowalewski, D.E., Baldwin, S.L., and Webb, L.E., 2006, The age and origin of the Labyrinth, western Dry Valleys, Antarctica: Evidence for extensive middle Miocene subglacial floods and freshwater discharge to the Southern Ocean: Geology, v. 34, no. 7, p. 153–156, https://doi.org/10.1130/G22145.1.

Lewis, A.R., Marchant, D.R., Ashworth, A.C., Hedenäs, L., Hemming, S.R., Johnson, J.V., Leng, M.J., Machlus, M.L., Newton, A.E., Raine, J.I., Willenbring, J.K., Williams, M., and Wolfe, A.P., 2008, Mid-Miocene cooling and the extinction of tundra in continental Antarctica: Proceedings of the National Academy of Sciences of the United States of America, v. 105, no. 31, p. 10676–10680, https://doi.org/10.1073/pnas.0802501105.

Licht, K.J., Lederer, J.R., and Jeffrey Swope, R., 2005, Provenance of LGM glacial till (sand fraction) across the Ross embayment, Antarctica: Quaternary Science Reviews, v. 24, no. 12, p. 1499–1520, https://doi.org/10.1016/j.quascirev.2004.10.017.

Lønne, I., and Nemec, W., 2011, The kinematics of ancient tidewater ice margins: criteria for recognition from grounding-line moraines, *in* Martini, I.P., French, H.M., and Pérez-Alberti, A., eds., Ice-Marginal and Periglacial Processes and Sediments: Geological Society of London, Special Publication 354, no. 1, p. 57–75, https://doi.org/10.1144/SP354.4.

Lonsdale, M.J., 1990, The relationship between silica diagenesis, methane, and seismic reflections on the South Orkney microcontinent, *in* Barker, P.F., and Kennett, J.P., eds., Proceedings of the Ocean Drilling Program Scientific Results, Weddell Sea, Antarctica: College Station, Texas, Deep Sea Drilling Project Reports and Publications, v. 113, p. 27–37, https://doi.org/10.2973/odp.proc.sr.113.177.1990.

McKay, R., Browne, G., Carter, L., Cowan, E., Dunbar, G., Krissek, L., Naish, T., Powell, R., Reed, J., Talarico, F., and Wilch, T., 2009, The stratigraphic signature of the late Cenozoic Antarctic Ice Sheets in the Ross Embayment: Geological Society of America Bulletin, v. 121, no. 11–12, p. 1537–1561, https://doi.org/10.1130/B26540.1.

McKay, R., Naish, T., Powell, R., Barrett, P., Scherer, R., Talarico, F., Kyle, P., Monien, D., Kuhn, G., Jackolski, C., and Williams, T., 2012, Pleistocene variability of Antarctic Ice Sheet extent in the Ross Embayment: Quaternary Science Reviews, v. 34, p. 93–112, https://doi.org/10.1016/j.quascirev.2011.12.012.

McKay, R., De Santis, L., Kulhanek, D.K., and the Expedition 374 Scientists, 2019, Ross Sea West Antarctic Ice Sheet History: Proceedings of the International Ocean Discovery Program: College Station, Texas, International Ocean Discovery Program, v. 374, https://doi.org/10.14379/iodp.proc.374.2019.

Miller, K.G., Browning, J.V., Schmelz, W.J., Kopp, R.E., Mountain, G.S., and Wright, J.D., 2020, Cenozoic sea-level and cryospheric evolution from deep-sea geochemical and continental margin records: Science Advances, v. 6, no. 20, https://doi.org/10.1126/sciadv.aaz1346.

Naish, T., Carter, L., Wolff, E., Pollard, D., and Powell, R., 2009, Late Pliocene–Pleistocene Antarctic climate variability at orbital and suborbital scale: Ice sheet, ocean and atmospheric interactions, *in* Florindo, F., and Siegert, M., eds., Developments in Earth & Environmental Sciences: London, UK, Elsevier, v. 8, p. 465–529.

Neagu, R.C., 2011, The relationship between biogenic silica diagenesis and the physical properties of sediments studied using seismic and well data [Ph.D. thesis]: Cardiff, UK, Cardiff University, 277 p.

Nobes, D.C., Murray, R., Kuramoto, S.i., Pisciotto, K.A., and Holler, P., 1992, Impact of silica diagenesis on physical property variations, *in* Pisciotto, K.A., Ingle, J.C, Jr., von Breymann, M.T., Barron, J., et al., eds., Proceedings of the Ocean Drilling Program, Scientific Results: College Station, Texas, Deep Sea Drilling Project Reports and Publications, v. 127-128, part 1, https://doi.org/10.2973/odp.proc.sr.127128-1.111.1992.

Passchier, S., Browne, G., Field, B., Fielding, C.R., Krissek, L.A., Panter, K., and Pekar, S.F., 2011, Early and middle Miocene Antarctic glacial history from the sedimentary facies distribution in the AND-2A drill hole, Ross Sea, Antarctica: Bulletin of the Geological Society of America, v. 123, no. 11–12, p. 2352–2365, https://doi.org/10.1130/B30334.1.

Patterson, M.O., McKay, R., Naish, T., Escutia, C., Jimenez-Espejo, F.J., Raymo, M.E., Meyers, S.R., Tauxe, L., Brinkhuis, H., Klaus, A., Fehr, A., Bendle, J.A.P., Bijl, P.K., Bohaty, S.M., Carr, S.A., Dunbar, R.B., Flores, J.A., Gonzalez, J.J., Hayden, T.G., Iwai, M., Katsuki, K., Kong, G.S., Nakai, M., Olney, M.P., Passchier, S., Pekar, S.F., Pross, J., Riesselman, C.R., Röhl, U., Sakai, T., Shrivastava, P.K., Stickley, C.E., Sugasaki, S., Tuo, S., van de Flierdt, T., Welsh, K., Williams, T., and Yamane, M., 2014, Orbital forcing of the East Antarctic ice sheet during the Pliocene and early Pleistocene: Nature Geoscience, v. 7, no. 11, p. 841–847, https://doi.org/10.1038/ngeo2273.

Paxman, G.J.G., Jamieson, S.S.R., Hochmuth, K., Gohl, K., Bentley, M.J., Leitchenkov, G., and Ferraccioli, F., 2019, Reconstructions of Antarctic topography since the Eocene–Oligocene boundary: Palaeogeography, Palaeoclimatology, Palaeoecology, v. 535, no. 109346, https://doi.org/10.1016/j.palaeo.2019.109346.

Payton, C.E., 1977, Seismic stratigraphy: Applications to hydrocarbon exploration: Tulsa, Oklahoma, USA, American Association of Petroleum Geologists, Memoir 26, 516 p.

Perotti, M., Andreucci, B., Talarico, F., Zattin, M., and Langone, A., 2017, Multianalytical provenance analysis of Eastern Ross Sea LGM till sediments (Antarctica): Petrography, geochronology, and thermochronology detrital data: Geochemistry, Geophysics, Geosystems, v. 18, no. 6, p. 2275–2304, https://doi.org/10.1002/2016GC006728.

Powell, R., and Cooper, J., 2002, A glacial sequence stratigraphic model for temperate, glaciated continental shelves, *in* Dowdeswell, J.A., and Cofaigh, C.O., eds., Glacier-Influenced Sedimentation on High-Latitude Continental Margins: Geological Society of London, Special Publication 203, p. 215–244, https://doi.org/10.1144/GSL.SP.2002.203.01.12.

Prothro, L.O., Simkins, L.M., Majewski, W., and Anderson, J.B., 2018, Glacial retreat patterns and processes determined from integrated sedimentology and geomorphology records: Marine Geology, v. 395, p. 104–119, https://doi.org/10.1016/j.margeo.2017.09.012.

Sangiorgi, F., Bijl, P.K., Passchier, S., Salzmann, U., Schouten, S., McKay, R., Cody, R.D., Pross, J., van de Flierdt, T., Bohaty, S.M., Levy, R., Williams, T., Escutia, C., and Brinkhuis, H., 2018, Southern Ocean warming and Wilkes Land ice sheet retreat during the mid-Miocene: Nature Communications, v. 9, no. 317, https://doi.org/10.1038/s41467-017-02609-7.

Sato, S., Asakura, N., Saki, T., Oikawa, N., and Kaneda, Y., 1984, Preliminary results of geological and geophysical surveys in the Ross Sea and in the Dumont D'Urville Sea, off Antarctica: Memoirs of National Institute of Polar Research Special Issue, v. 33, p. 66–92.

Savage, M.L., and Ciesielski, P.F., 1983, A revised history of glacial sedimentation in the Ross Sea region, *in* Oliver, R.L., James, P.R., and Jago, J.B., eds., Antarctic Earth Science: Canberra, Australia, Australian Academy of Science, p. 555–559.

Shackleton, N.J., and Kennett, J.P., 1975, Paleotemperature history of the Cenozoic and the initiation of Antarctic Glaciation: Oxygen and carbon isotope analyses in DSDP sites 272, 279, and 281, *in* Kennett, J.P., Houtz, R.E., Andrews, P.B., Edwards, A.R., Gostin, V.A., Hajós, M., Hampton, M.A., Jenkins, D.G., Margolis, S.V., Ovenshine, A.T., and Perch-Nielsen, K., Initial Reports of the Deep Sea Drilling Project: College Station, Texas, Deep Sea Drilling Project Reports and Publications, v. 29, p. 743–755, https://doi.org/10.2973/dsdp.proc.29.117.1975.

Shevenell, A.E., Kennett, J.P., and Lea, D.W., 2004, Middle Miocene Southern Ocean cooling and Antarctic cryosphere expansion: Science, v. 305, no. 5691, p. 1766–1770, https://doi.org/10.1126/science.1100061.

Shevenell, A.E., Kennett, J.P., and Lea, D.W., 2008, Middle Miocene ice sheet dynamics, deep-sea temperatures, and carbon cycling: A Southern Ocean perspective: Geochemistry, Geophysics, Geosystems, v. 9, no. 2, https://doi.org/10.1029/2007GC001736.

Shipp, S., Anderson, J., and Domack, E., 1999, Late Pleistocene–Holocene retreat of the West Antarctic Ice-Sheet system in the Ross Sea: Part 1: Geophysical results: Geological Society of America Bulletin, v. 111, no. 10, p. 1486–1516, https://doi.org/10.1130/0016-7606(1999)111<1486:LPHROT>2.3.CO;2.

Sugden, D., and Denton, G., 2004, Cenozoic landscape evolution of the Convoy Range to Mackay Glacier area, Transantarctic Mountains: Onshore to offshore synthesis: Geological Society of America Bulletin, v. 116, no. 7–8, p. 840–857, https://doi.org/10.1130/B25356.1.

Sugden, D.E., Marchant, D.R., and Denton, G.H., 1993, The case for a stable East Antarctic Ice Sheet: The background: Geografiska Annaler. Series A. Physical Geography, v. 75, no. 4, p. 151–154, https://doi.org/10.1080/04353676.1993.11880392.

Summerfield, M.A., Stuart, F.M., Cockburn, H.A.P., Sugden, D.E., Denton, G.H., Dunai, T.J., and Marchant, D.R., 1999, Long-term rates of denudation in the Dry Valleys, Transantarctic Mountains, southern Victoria Land, Antarctica bases on in-situ-produced cosmogenic ^{21}Ne: Geomorphology, v. 27, p. 113–129, https://doi.org/10.1016/S0169-555X(98)00093-2.

Tada, R., 1991, Origin of rhythmical bedding in middle Miocene siliceous rocks of the Onnagawa Formation,

northern Japan: Journal of Sedimentary Petrology, v. 61, no. 7, p. 1123–1145.

Tinto, K.J., Padman, L., Siddoway, C.S., Springer, S.R., Fricker, H.A., Das, I., Caratori Tontini, F., Porter, D.F., Frearson, N.P., Howard, S.L., Siegfried, M.R., Mosbeux, C., Becker, M.K., Bertinato, C., Boghosian, A., Brady, N., Burton, B.L., Chu, W., Cordero, S.I., Dhakal, T., Dong, L., Gustafson, C.D., Keeshin, S., Locke, C., Lockett, A., O'Brien, G., Spergel, J.J., Starke, S.E., Tankersley, M., Wearing, M.G., and Bell, R.E., 2019, Ross Ice Shelf response to climate driven by the tectonic imprint on seafloor bathymetry: Nature Geoscience, v. 12, no. 6, p. 441–449, https://doi.org/10.1038/s41561-019-0370-2.

Tribble, J.S., Mackenzie, F.T., Urmos, J., O'Brien, D.K., and Manghnani, M.H., 1992, Effects of biogenic silica on acoustic and physical properties of clay-rich marine sediments: The American Association of Petroleum Geologists Bulletin, v. 76, no. 6, p. 792–804.

Tuzzi, E., 2009, Advances in Neogene Antarctic diatom biostratigraphy [Ph.D. thesis]: Lincoln, Nebraska, University of Nebraska, 168 p.

Warny, S., Askin, R.A., Hannah, M.J., Mohr, B.A.R., Raine, J.I., Harwood, D.M., and Florindo, F., and the SMS Science Team, 2009, Palynomorphs from a sediment core reveal a sudden remarkably warm Antarctica during the middle Miocene: Geology, v. 37, no. 10, p. 955–958, https://doi.org/10.1130/G30139A.1.

Wilson, D.S., Jamieson, S.S.R., Barrett, P.J., Leitchenkov, G., Gohl, K., and Larter, R.D., 2012, Antarctic topography at the Eocene–Oligocene boundary: Palaeogeography, Palaeoclimatology, Palaeoecology, v. 335–336, p. 24–34, https://doi.org/10.1016/j.palaeo.2011.05.028.

Wilson, D.J., Bertram, R.A., Needham, E.F., van de Flierdt, T., Welsh, K.J., McKay, R.M., Mazumder, A., Riesselman, C.R., Jimenez-Espejo, F.J., and Escutia, C., 2018, Ice loss from the East Antarctic Ice Sheet during late Pleistocene interglacials: Nature, v. 561, no. 7723, p. 383–386, https://doi.org/10.1038/s41586-018-0501-8.

You, Y., Huber, M., Müller, R. D., Poulsen, C. J., and Ribbe, J., 2009, Simulation of the Middle Miocene Climate Optimum: Geophysical Research Letters, v. 36, no. 4, https://doi.org/10.1029/2008GL036571.

Zachos, J., Pagani, H., Sloan, L., Thomas, E., and Billups, K., 2001, Trends, rhythms, and aberrations in global climate 65 Ma to present: Science, v. 292, no. 5517, p. 686–693, https://doi.org/10.1126/science.1059412.

Science Editor: Rob Strachan
Associate Editor: Michael Smith

Manuscript Received 1 July 2020
Revised Manuscript Received 14 January 2021
Manuscript Accepted 15 March 2021

Printed in the USA